Volume 8 | Number 3 | March 2015 | Pages 677–1048

Energy & Environmental Science

www.rsc.org/ees

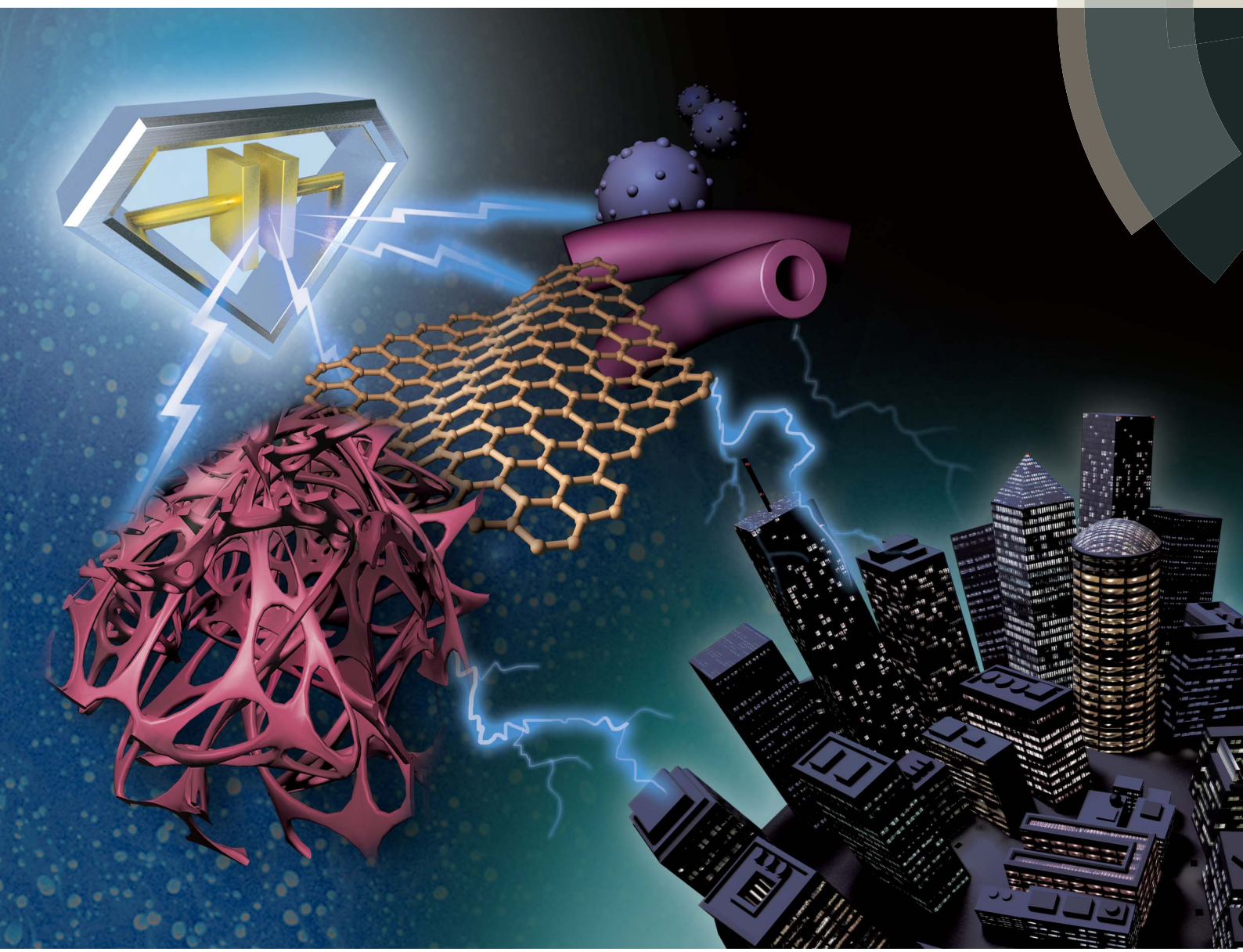

ISSN 1754-5692

ROYAL SOCIETY OF CHEMISTRY

REVIEW ARTICLE

Jayan Thomas *et al.*

Supercapacitor electrode materials: nanostructures from 0 to 3 dimensions

Energy & Environmental Science

REVIEW

View Article Online
View Journal | View Issue

Cite this: *Energy Environ. Sci.*, 2015, **8**, 702

Supercapacitor electrode materials: nanostructures from 0 to 3 dimensions

Zenan Yu, Laurene Tetard, Lei Zhai and Jayan Thomas*

Received 11th October 2014
Accepted 28th November 2014

DOI: 10.1039/c4ee03229b

www.rsc.org/ees

Supercapacitors have drawn considerable attention in recent years due to their high specific power, long cycle life, and ability to bridge the power/energy gap between conventional capacitors and batteries/fuel cells. Nanostructured electrode materials have demonstrated superior electrochemical properties in producing high-performance supercapacitors. In this review article, we describe the recent progress and advances in designing nanostructured supercapacitor electrode materials based on various dimensions ranging from zero to three. We highlight the effect of nanostructures on the properties of supercapacitors including specific capacitance, rate capability and cycle stability, which may serve as a guideline for the next generation of supercapacitor electrode design.

Broader context

The ever-growing global demand of energy together with the depletion of fossil fuels makes it critical to develop sustainable and renewable energy resources. Developing relevant energy storage systems (*e.g.* batteries and supercapacitors) is essential to utilizing sustainable and renewable energy resources. A supercapacitor is highly beneficial in storing renewable energy. For example, when light is not shining or wind is not blowing, the energy needs to be stored in devices like batteries and supercapacitors. Among the efforts of building efficient supercapacitors, electrode materials with rational nanostructured designs have offered major improvements in performance over the past several years. This review article is intended to examine recent progress in nanostructuring supercapacitor electrode materials, highlighting the fundamental understanding of the relationship between structural properties and electrochemical performances, as well as an outlook on the next generation of nanostructured supercapacitor electrodes design.

1 Introduction

Before a ray of sun light peeked through the curtain and shined on John's face, everything was perfect for a quiet morning. Suddenly jumping off the bed, "Oh, my, I forgot to set the alarm last night." He got dressed and rushed to his electric car; "LOW BATTERY" exclaimed John, "wish I could charge it up in a few minutes…" As a matter of fact, such energy storage technologies like supercapacitors which can charge very quickly have been around for decades, but their low energy densities have held them back in many such applications. The ever growing demand for energy urges researchers to look for new materials and processes to develop highly improved energy storage devices. Among energy storage systems, supercapacitors have drawn considerable attention during recent years due to their fast charge–discharge characteristics, high power density, and excellent cycle stability. Currently, supercapacitors are used along with batteries to provide the additional power required in many applications. However, they cannot be used as stand-alone units in these applications since their energy density is inferior to that of batteries. For example, commercially available supercapacitors can provide energy densities of less than 10 W h Kg^{-1} whereas Li-ion batteries can provide energy densities of more than 180 W h Kg^{-1}.[1,2] Nevertheless, the power density and cycle life of supercapacitors are far superior to those of Li-ion batteries. At present, the scientific community is striving to considerably improve the energy and power density of supercapacitors by developing new electrode materials and electrolytes, and ingenious device design.

Achieving noteworthy improvements in supercapacitor performances by means of better electrode materials together with low-cost and environment-friendly production, requires a deep fundamental understanding of the charge storage mechanisms, transport pathways of electrons and ions, and electrochemically active sites. Advances in nanomaterials, ideal candidates for improved ion adsorption or faster surface redox reactions, have fostered extensive research efforts toward the enhancement of electrochemically active sites for charge transfer and controlled ionic and electronic transport at small diffusion length scales.

Supercapacitors are generally classified into two types based on their storage mechanism, the electrochemical double layer capacitors (EDLCs) and pseudocapacitors. EDLCs physically store charges *via* reversible ion adsorption at the electrode–electrolyte interface, while pseudocapacitors chemically store

NanoScience Technology Center (NSTC), Department of Materials Science and Engineering, Department of Physics, Department of Chemistry, College of Optics and Photons, University of Central Florida, Orlando, FL 32826, USA. E-mail: Jayan.Thomas@ucf.edu; Fax: +1 407 882 2819; Tel: +1 407 882 0196

their charges *via* redox reaction at the vicinity (a few nanometers) of the surface. Typically, electrode materials for EDLCs are made of carbon-based materials (including activated carbon, carbon nanotubes, graphene, *etc.*), while that for pseudocapacitors are transition metal oxides (*e.g.* RuO_2, MnO_2, CoO_x, NiO, Fe_2O_3, *etc.*) and conducting polymers (*e.g.* polypyrrole, polyaniline, poly(3,4-ethylenedioxythiophene), *etc.*).

The criteria for designing a high-performance supercapacitor electrode include high specific capacitance (energy stored per unit mass, volume, or area of active materials), large rate capability (capacitance retention at high scan rate or current density), and high cycle stability. In addition, the toxicity and cost of the active materials used in an electrode design should be taken into account as well. Therefore, in order to realize a high-performance supercapacitor electrode, factors that determine the specific capacitance, rate capability, and cycle stability need to be mentioned here. (1) Surface area: Since charges are stored on the surface of the supercapacitor electrodes, an electrode with a higher surface area leads to an improved specific capacitance. Nanostructuring of electrode materials is a feasible method to considerably improve the surface area of the electrodes. (2) Electronic and ionic conductivity: As specific capacitance and rate capability are considerably dependent on both electronic and ionic conductivity, a high electronic and ionic conductivity will help to maintain the rectangular nature of cyclic voltammetry (CV) curve and symmetricity of galvanostatic charging–discharging (GCD) curves. They also reduce the specific capacitance losses as scan rates/current densities are increased. Typical approaches to enhance the electronic conductivity include binder-free electrode design and nanostructured current collector design to provide efficient electron pathways for charge transport. To increase the ionic conductivity, precise control of pore size and prudent design strategies are used (*e.g.* more open structures for ion transport). (3) Mechanical and chemical stability: The cycle stability is greatly influenced by the mechanical and chemical stability of electrode materials during

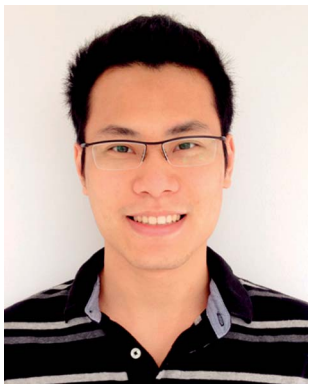

Zenan Yu is a Ph.D. student in the Department of Materials Science and Engineering at University of Central Florida. He received his B.S. degree in Electronic Science and Technology from Shanghai University in 2011. Under the supervision of Professor Jayan Thomas, his research interests mainly focus on the design, synthesis and applications of nanostructured materials for supercapacitors.

Lei Zhai is an associate professor at the NanoScience Technology Center (NSTC) and Department of Chemistry. He received his Ph.D. from Carnegie Mellon University in 2002 and worked as a postdoctoral research associated at Massachusetts Institute of Technology before he joined the University of Central Florida in 2005. He is a recipient of NSF CAREER Award and a Scialog Fellow of Research Corporation for Science Advancement. His research focuses on conjugated polymers and composites for energy conversion and storage, surface science and engineering, and polymer derived ceramics.

Laurene Tetard is an assistant professor at the NanoScience Technology Center (NSTC) and Department of Physics. She received her B.S. and M.S. from the University of Burgundy in France and completed her Ph.D. with Professor Thundat at the University of Tennessee, Knoxville in 2010. She was a Eugene P. Wigner Fellow at the Oak Ridge National Laboratory from 2011 to 2013 before joined the University of Central Florida in 2013. Her current research interest includes innovative nanoscale characterization of energy-related materials including two dimensional materials and soft matter.

Jayan Thomas is an assistant professor at the NanoScience Technology Center (NSTC), College of Optics and Photonics (CREOL) and College of Engineering and Computer Science at the University of Central Florida (UCF). After receiving Ph.D. from Cochin University of Science and Technology in India, he joined College of Optical Sciences, University of Arizona in 2001 as a research faculty. He moved to UCF in 2011 and is currently working on the development of supercapacitors, photorefractive polymers and solar cells. He is a recipient of NSF CAREER award, VEECO's 2010 best nanotechnology innovation award and WTN World Technology (Energy) Award-2014 sponsored by FORTUNE and TIME.

cycling. Phase change, dissolution, and side reaction of active materials are the major reasons for causing cycle instability. Sensible electrode surface protection may substantially boost the cycle stability. In addition to investigating new electrode materials, electrode design with nanostructures offers a promising avenue to fulfill high-performance supercapacitors. This is because the aforementioned factors can be effectively manipulated by a nanostructured design, which will be discussed in detail in the following sections.

Typically, nanomaterials can be classified into zero dimensional (0D), one dimensional (1D), two dimensional (2D) and three dimensional (3D) categories.[3–5] Particles which are more or less spherical in shape like fullerenes, quantum dots, nano-onions, nanoparticles, *etc.* are considered as 0D. Nanostructures with 1D are interesting due to their dimensionality dependence on its functional properties. They include nanotubes, nanofibers, nanowires, nanopillars, nanoribbons and nanobelts. Typically, materials with a thickness of a few atomic layers and with the other two dimensions beyond the nanometric size range are considered as 2D materials. Graphene and many other layered van der Waals solids like MoS_2, $CaGe_2$ and $CaSi_2$, fall under the 2D category. Materials with three dimensions beyond the nanometric size range but still preserve the advantages of nano size effect are regarded as 3D materials. Mesoporous carbon and graphene aerogel fall under 3D category.

Even though there are several reviews describing the material aspects of supercapacitor electrodes,[2,6–9] a comprehensive review of 0D, 1D, 2D and 3D materials used only in supercapacitors is still lacking. Although Wu and co-authors have reported the dimensional study of electrodes for 0 to 3D,[10] they only focused on carbon–metal oxide composite electrodes from 0 to 3D. This review covers a much broader range of electrode materials. In recent years, a range of materials configurations ranging from 0D particles to 3D nanostructured frameworks have been developed and tested in supercapacitors devices. This review is aiming to fill this gap and provide the readers a clear idea about the performance of these materials as electrodes in electrochemical supercapacitors. Fig. 1 summarized the key points of electrode materials from 0 to 3D and a detailed discussion is given in the following sections.

2 0D nanostructures

According to the strict definition, 0D nanostructures are spherical particles that have three dimensions constrained on the nanoscale (usually 1–100 nm). Nevertheless, particles with diameters up to 1 μm are usually regarded as nanoparticles as well, as the benefit provided by the effect of their small size has been observed for this size range. In this section, three subcategories of 0D nanostructures used as electrodes in supercapacitors are considered, *viz.*, solid, hollow, and core–shell 0D nanostructures.

2.1 Solid 0D nanostructures

As the foundation of 0D nanostructures, solid nanoparticles (nanospheres) are intensely investigated for designing supercapacitor electrodes. Carbon materials (*e.g.* activated carbon,[11] carbon nanospheres,[12] and mesoporous carbon[13,14]) and transition metal oxides (*e.g.* MnO_2,[15,16] NiO,[17–19] Fe_3O_4,[20] *etc.*) have been widely fabricated into solid nanoparticles for electrode materials. Among carbon materials, activated carbons (ACs) are distinct due to their high surface area (up to 3000 $m^2\ g^{-1}$) and economical fabrication process. In addition, ACs propose a wide range of pore size distribution including micropores (<2 nm), mesopores (2–50 nm), and macropores (>50 nm).[21] ACs are generally produced by either physical or chemical activation of versatile carbonaceous precursors such as wood, coal, nutshell, and so forth. Larger surface area is usually expected to result in a higher specific capacitance. However, even with a surface area of up to 3000 $m^2\ g^{-1}$, only small specific capacitance (<10 $\mu F\ cm^{-2}$) could be obtained with ACs.[1] This is due to the fact that specific capacitance is not only determined by surface area but also by other parameters such as pore size distribution, pore shape and structure, accessibility of the electrolyte, and electrical conductivity.[6] Therefore, an ideal design of ACs should meet at least two requirements: (1) large surface area for the enhancement of electrochemically active sites and (2) suitable pore size and structure for the transportation of ions in the electrolyte. In addition to ACs, Gogotsi, Simon, and their co-workers have prepared onion-like carbon by annealing nanodiamond powder at 1800 °C.[22,23] The carbon onions were found to possess a moderate specific surface area (~500 $m^2\ g^{-1}$) compared to ACs; however, the surface can be fully accessed by ions (Fig. 2). As a result, micro-supercapacitors based on these onion-like carbons showed ~70% rate capability from 1 to 100 V s^{-1} and an excellent relaxation time constant (26 ms) compared to that of activated carbon (700 ms).

The above mentioned criteria for designing ideal ACs are also applicable to transition metal oxide nanoparticles in pseudocapacitors as they rely on fast surface redox reactions. Additionally, as most of the transition metal oxides suffer from poor electrical conductivity, enhancing the bulk electrical conductivity should also be taken into account. For example, Chen and co-workers have fabricated nanoporous metal/oxide hybrid supercapacitor electrodes in order to enhance the electrical conductivity of MnO_2.[24] In this method, conductive nanoporous gold was first produced by de-alloying $Ag_{65}Au_{35}$ using HNO_3, followed by growing nanocrystalline MnO_2 (with a grain size of ~5 nm) into the nanopores. The resulting nanoporous Au/MnO_2 supercapacitor electrode showed a high specific capacitance of ~1145 F g^{-1} at 50 mV s^{-1}, which can be attributed to nanoporous gold that allows easy and efficient access to both electrons and ions. Recent advances in using perovskite materials for solar energy harvesting have greatly stimulated the enthusiasm of researchers to exploit these materials for other potential fields. Lately, Stevenson, Johnston, and co-workers have prepared $LaMnO_3$ nanoparticles *via* reverse-phase hydrolysis method as supercapacitor electrode material.[25] Fig. 3a shows an ideal $LaMnO_3$ cubic perovskite structure, where lanthanum atom locates at body centered position, manganese atoms at cubic corner positions, and oxygen atoms at mid-edge positions respectively. The dark-field SEM image (Fig. 3b) presents the small (~20–50 nm)

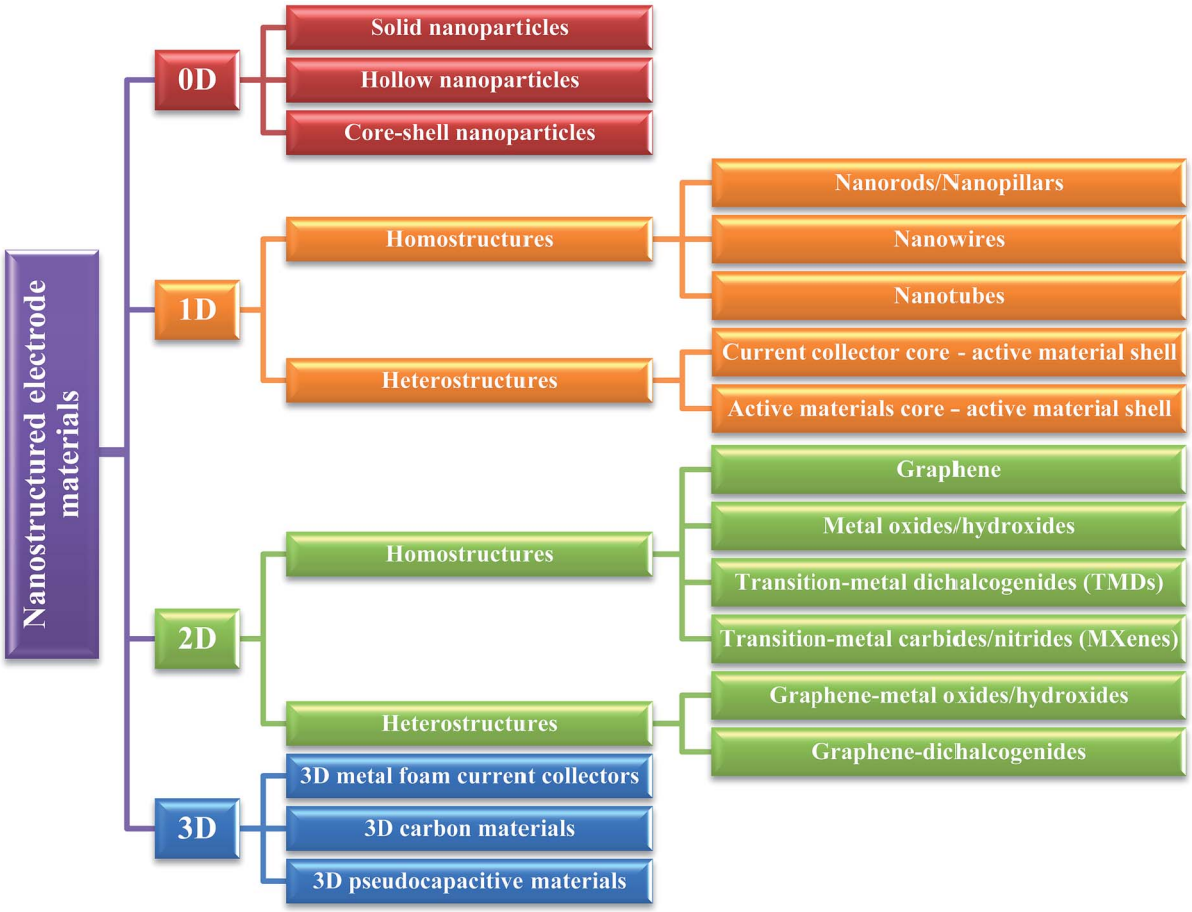

Fig. 1 A schematic representation summarizing the key aspects of electrode materials from 0 to 3D.

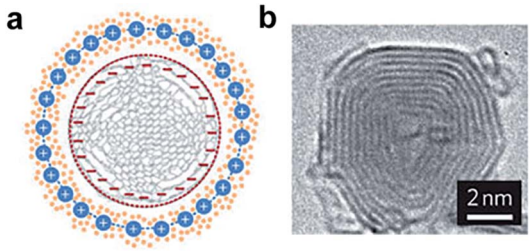

Fig. 2 (a) Cross-section of a charged 0D onion-like carbon capacitor. (b) TEM image of a carbon onion with lattice spacing close to 0.35 nm. Reproduced with permission from ref. 23. Copyright 2010 Macmillan Publishers Limited.

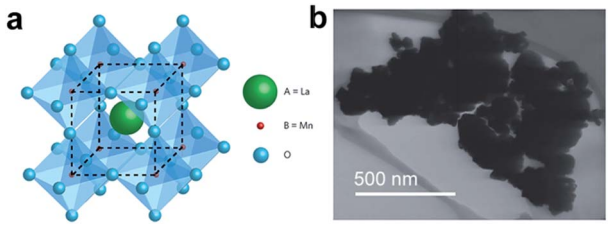

Fig. 3 (a) Idealized cubic $LaMnO_3$ perovskite structure. (b) Dark-field SEM image of $LaMnO_{3.09}$ nanoparticles. Reproduced with permission from ref. 25. Copyright 2014 Macmillan Publishers Limited.

nanocrystals of $LaMnO_{3.09}$ that were sintered into agglomerated particles. They have found that oxygen intercalation has significant effect on $LaMnO_3$ perovskite nanoparticles as supercapacitor electrodes. The specific capacitances of $LaMnO_{3.09}$ and $LaMnO_{2.91}$ reached 586.7 and 609.8 F g^{-1}, respectively. Interestingly, the capacitance difference (~4%) was found to be close to the oxygen content difference (~6%), implying that the oxygen intercalation is the major charge storage mechanism of $LaMnO_3$ perovskite supercapacitor electrodes. This assumption was further demonstrated by applying electrolyte with varying anion concentrations as well as different electrolyte types (*i.e.* neutral and alkaline electrolytes). As a result, perovskite-type materials with anion vacancies can be exploited to store charge through oxygen intercalation. Therefore, in addition to traditional solid 0D active materials (*e.g.* activated carbon), perovskite materials might open a new paradigm as supercapacitor electrode materials.

2.2 Hollow 0D nanostructures

Hollow 0D nanostructures have been recognized as promising candidates for electrode design due to their peculiar properties

such as low density, high surface-to-volume ratio and shortened pathways for transporting both mass and charges.[26] Hollow 0D nanostructures are generally synthesized *via* three distinct approaches: hard templating, soft templating, and template-free methods. Among them, hard templating methods have been widely adopted because of their remarkable advantages in controlling the size, shape, and structure of the products.[27] Typically, a single-shelled hollow nanosphere is created by coating a thin layer of precursor materials onto a spherical hard template (*e.g.* silica spheres, polystyrene colloid spheres, carbonaceous spheres, *etc.*), followed by removing the template either by calcination or by chemical etching. For example, Yang and co-workers reported the synthesis of hollow carbon nanospheres by carbonizing its hollow nanosphere precursor obtained through a silica sphere-assisted hard templating method.[28] The resulting hollow carbon nanospheres showed a high surface area (1704 m^2 g^{-1}), large bimodal mesopores (6.4 and 3.1 nm), and large pore volumes (1.6 cm^3 g^{-1}). With such a design, a specific capacitance of 251 F g^{-1} at 50 mV s^{-1} was achieved for the hollow carbon nanospheres. Hollow 0D structures based on other electrode materials such as MnO_2,[29,30] NiO,[31,32] NiS,[33] *etc.* have been investigated as well.

In addition to single shelled hollow 0D nanostructures, multiple shelled samples have also shown fascinating characteristics (*e.g.* substantially improved surface-to-volume-ratio) for efficient electrode material design. Similarly, electrode materials like NiO,[34] Co_3O_4,[35] and Fe_2O_3,[36] have been successfully fabricated into multi-shelled structures. For example, Zhang and co-workers reported the synthesis of NiO hollow nanospheres *via* layer-by-layer (LBL) self-assembly for supercapacitor application.[34] In their method, the number of shells was directly determined by the cycles of immersion–precipitation process before removing the carbonaceous template *via* calcination (Fig. 4a). Single, double, and triple shelled NiO nanospheres were prepared by repeating the immersion–precipitation process for 0, 1, and 2 times (Fig. 4b and c). The double-shelled NiO nanospheres exhibited the highest surface area (92.00 m^2 g^{-1}), which ascribes to their more loosely-packed structure compared to their single and triple shelled counterparts. As a result, the double shelled NiO nanospheres showed the most enhancement in specific capacitance (612.5 F g^{-1}). Since many other promising electrode materials have not been fabricated into 0D multi shelled structures, much effort still needs to be dedicated in the future.

2.3 Core–shell 0D nanostructures

Core–shell 0D nanostructures often refer to a solid or hollow nanoparticle coated with a thin shell. Combining faradaic and non-faradaic materials into core–shell 0D nanostructures offer considerable advantages including enhanced electrical conductivity, less agglomeration, robust chemical and mechanical stability, *etc.*[37–40] For example, Zhao and co-workers have grown conducting polymer (polyaniline (PANI)) on hollow carbon spheres as supercapacitor electrode materials.[37] Hollow carbon spheres (HCS) with high specific area (2239 m^2 g^{-1}) were first prepared using ferrocene as the carbon precursor and silica

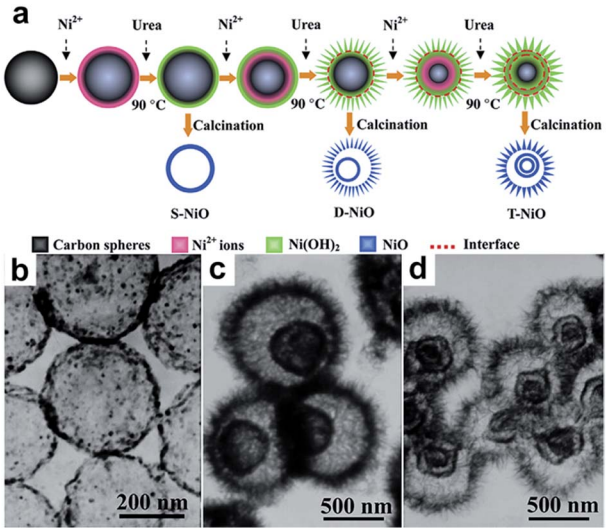

Fig. 4 (a) Schematic of synthesizing multishelled NiO hollow nanospheres using LBL self-assembly. TEM images show NiO hollow nanospheres with (a) single-shell, (b) double-shells, and (c) triple-shells. Reproduced with permission from ref. 34. Copyright 2014 Elsevier.

spheres as the template. PANI was then conformally grown on the surface of the HCS by polymerizing aniline at room temperature for 12 h (Fig. 5a and b). HCS–PANI core–shell structures with an optimized content of PANI showed a specific capacitance of 525 F g^{-1}, which is almost two times greater than that of pristine HCS (268 F g^{-1}). However, the rate capability of HCS–PANI decayed with increasing PANI content, which can be attributed to the pore blockage due to the reduced accessibility of electrolyte ions. Zhao's group also synthesized core–shell nanoparticles with carbon core and MnO_2 shell by direct redox reaction between graphitic hollow carbon spheres (GHCS) and $KMnO_4$ solution at 70 °C (Fig. 5c and d).[38] The as-prepared

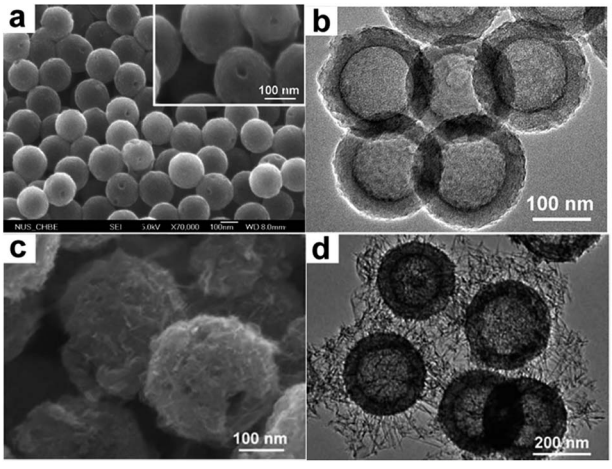

Fig. 5 (a) FESEM and (b) TEM images of HCS–PANI. (c) FESEM and (d) TEM images of GHCS–MnO_2. Reproduced with permission from ref. 37 and 38. Copyright: 2010 American Chemical Society and 2012 The Royal Society of Chemistry.

GHCS–MnO_2 core–shell nanostructures showed a maximum specific capacitance of 190 F g^{-1} at 0.1 A g^{-1} with an optimized MnO_2 content (64 wt%), more than two times higher than that of pristine GHCS (95 F g^{-1}). Moreover, the GHCS–MnO_2 core–shell nanostructures maintained 55% capacitance retention while current density increased from 0.1 to 10 A g^{-1}, indicating a porous structure of MnO_2 shell was formed to provide efficient diffusion pathway for electrolyte ions.

3 1D nanostructures

1D nanostructures are slivers of material with two dimensions constrained on nanoscale.[41] They have been extensively studied for the design of electrode materials for supercapacitors due to their unique and superior chemical and physical properties.[42–47] For instance, the longitudinal axis of 1D nanostructures can provide efficient transport pathway for both electrons and ions,[48] while maintaining the similar benefits of 0D nanostructures in the two nanoscale dimensions. In this section, we place 1D nanostructures into two major categories: homostructures and heterostructures.

3.1 1D homostructures

1D homostructures are structures with only one singular structure such as nanorods, nanowires, nanotubes, *etc.* They can be divided into three groups, namely, nanorods/nanopilars with aspect ratios (length/diameter) less than 10, nanowires with aspect ratios more than 10, and nanotubes with hollow interiors.[49] The methods for synthesizing 1D homostructures are versatile and can generally be divided into two major types, template-assisted and template-free methods. For template-assisted methods, sacrificial templates (*e.g.* AAO templates) are commonly used to shape the initial structure, followed by the removal of the templates with an acidic or basic solution. For template-free methods, various approaches like hydrothermal synthesis, chemical vapor deposition (CVD), and electrodeposition are generally employed to directly grow 1D homostructures. Recently, vertical growth of active material on the conductive substrate either by a "bottom-up" or "top-down" method has become one of the most promising electrode design approaches. Such a design guarantees efficient transport of electrons between current collector and active material because of the binder-free design. It also enables fast transfer of ions between electrolyte and active materials because of the available void space between adjacent nanostructures.

3.1.1 Nanorods/nanopillars. Although the moderate aspect ratio of nanorods/nanopillars limits the enhancement of surface area compared to nanowires/nanofibers, the significantly lower chances for individual nanorod/nanopillar to collapse on to its neighboring structures making them more accessible to the electrolyte, which effectively increases the ionic conductivity.

Tong and co-workers have reported oxygen-deficient Fe_2O_3 nanorods as supercapacitor electrode material.[50] Nanorod-like FeOOH was first hydrothermally synthesized in an aqueous solution containing ferric chloride, sodium nitrate, and hydrogen chloride. Subsequently, the FeOOH nanorods were heated at high temperature in air and N_2, separately, which resulted in pristine Fe_2O_3 nanorods and oxygen-deficient Fe_2O_3 nanorods. Interestingly, the oxygen-deficient Fe_2O_3 nanorods exhibited more than two times enhancement of the specific capacitance (64.5 F g^{-1}) than that of pristine Fe_2O_3. This phenomenon may be attributed to the existence of oxygen vacancies which considerably enhance the donor density and in turn improve the conductivity and reactivity of Fe_2O_3 nanorods.

Recently, Thomas and co-workers reported a facile method to produce highly ordered carbon nanopillars as supercapacitor electrodes.[51] They first developed a novel technique, called spin-on nanoimprinting (SNAP), to print highly ordered polymer nanostructures.[51–54] In a typical SNAP process, a thin layer of polymer solution was spin-coated on an e-beam etched nanohole structured silicon mold, followed by curing and peeling off the polymer from the template (Fig. 6a). The SNAP technique was demonstrated to be simple, quick, and cost-effective since it requires just a spin coater and a pre-fabricated template. The entire printing process can be completed within a few minutes, but can be performed at a much faster pace if automated. Moreover, a large-scale nanostructure can be easily obtained by stitching several printed structures next to each other. Unlike commonly used sacrificial template (*e.g.* AAO template), this template can be re-used many times without any noticeable degradation of nanostructures since all the polymer nanopillars can easily be removed from the template. The carbon nanopillar arrays were obtained upon post stabilization and carbonization of the polymer nanostructures. Fig. 6b and c show the SEM images of printed polyacrylonitrile (PAN) and carbon nanopillar array. The diameter and height of each carbon nanopillar is ~95 nm and ~200 nm, respectively. Significantly, the specific capacitance of the carbon nanopillar arrays (3.4 mF cm^{-2}) showed considerable enhancement compared to that of a planar carbon film (0.05 mF cm^{-2}).

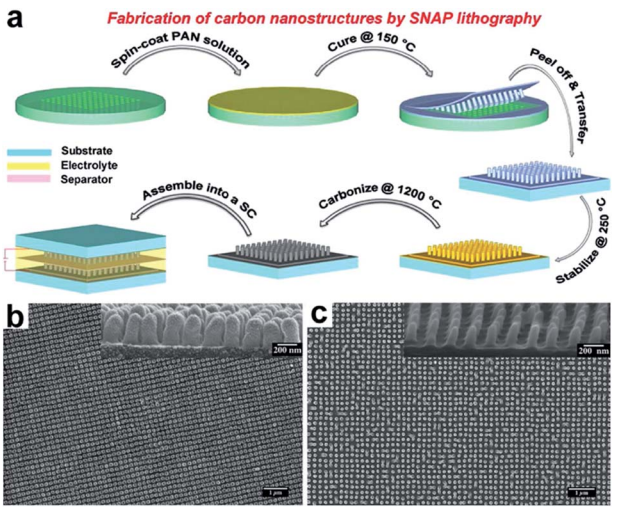

Fig. 6 (a) Fabrication of carbon nanostructures by SNAP method. (b) SEM images of top view and side view (inset) of polymer nanopillars. (c) SEM images of top view and side view (inset) of carbon nanopillars. Reproduced with permission from ref. 51. Copyright 2013 WILEY-VCH Verlag GmbH & Co. KGaA, Weinheim.

3.1.2 Nanowires. Nanowires have been widely studied as electrode material due to their high aspect ratio that can provide large surface area to store charges and an efficient pathway to transport charges. Taking PANI nanowires as an example, Li and co-workers have synthesized vertically aligned PANI nanowires as supercapacitor electrodes by means of electrochemical deposition using AAO templates.[55] The electrochemical deposition was carried out at a constant potential of 0.75 V for 5000 s in an electrolyte solution containing aniline and sulfuric acid. PANI nanowire arrays were obtained upon removing the AAO template in a 0.01 M NaOH solution. These samples showed a specific capacitance of 1142 F g^{-1} at a current density of 5 A g^{-1}, with 5% capacitance fading after 500 cycles. Regardless of the superior electrochemical performance of PANI nanowires, the usage of AAO templates limits the practicality of this fabrication process for large scale production since a new AAO template is required for every array of nanostructures produced. Lately, Wei and co-workers reported a facile one-step template-free approach to synthesize PANI nanowire arrays.[56] In their method, PANI nanowire could directly be electropolymerized by a simple galvanostatic deposition process at a constant current of 0.01 mA cm^{-2} for 1 h. Consequently, the as-prepared PANI nanowire arrays showed 950 F g^{-1} at a current density of 1 A g^{-1} and 16% loss after 500 cycles.

Lately, a ternary metallic oxide, spinel nickel cobaltite ($NiCo_2O_4$), has attracted substantial attention due to its high conductivity (more than two orders of magnitude higher than single NiO or Co_3O_4) and multiple oxide states that enable rich redox reactions originating from both nickel and cobalt ions.[57,58] For example, Lou and co-workers have successfully grown $NiCo_2O_4$ nanoneedle arrays directly on conductive substrates as supercapacitor electrodes.[59] In their synthetic process, a conductive substrate was first immersed into a solution containing nickel nitrite, cobalt nitrite, ethanol, and water in an appropriate ratio and heated to 85 °C for 8 h, followed by annealing at 250 °C for 90 min. Remarkably, the $NiCo_2O_4$ nanoneedle arrays showed a capacitance of 1118.6 F g^{-1} and about 10.6% loss in capacitance after 2000 cycles.

3.1.3 Nanotubes. Compared to solid nanostructures (*e.g.* nanowires), tubular nanostructures typically offer higher surface area with less utilization of mass, resulting in more gravimetric specific capacitance. Nanotubes are usually synthesized *via* template-assisted method, CVD, hydrothermal method, *etc.* For template-assisted method, nanotubes can be easily prepared by partially infiltrating the nanotube forming material into a nanoporous template. This is due to the fact that materials preferentially anchor on the walls of nanochannels at their early infiltrating stage. Therefore, it is critical to manipulate the infiltration process in order to produce tubular nanostructures. For example, MnO_2 nanotube arrays were synthesized using AAO template *via* electrochemical deposition for 10 min; whereas MnO_2 nanowire arrays were obtained after 60 min of deposition.[60] The MnO_2 nanotube arrays showed a specific capacitance of 320 F g^{-1}, while only 101 F g^{-1} was measured for the nanowire arrays. Using the same strategy, other electrode materials were synthesized with tubular nanostructure such as RuO_2,[61] PEDOT,[62] *etc.*

The discovery of carbon nanotubes (CNTs) has led to several applications in energy storage field. CNTs as supercapacitor electrode materials, and especially vertically aligned CNTs directly grown on conductive substrates, have drawn remarkable attention due to their moderate to high surface area (120–500 m^2 g^{-1}), porous structure, superior electronic conductivity, and excellent mechanical and thermal stability. Ajayan and co-workers have grown aligned CNTs (400 μm long) on metal alloy (Inconel) using vapour-phase catalyst delivery.[63] The CV curves showed rectangular and symmetric shape even at a scan rate of 1000 mV s^{-1}, suggesting ideal capacitive behavior and low contact resistance between the CNTs and the substrate. The specific capacitance of a supercapacitor based on these vertically aligned CNT arrays was found to be 18 F g^{-1}. Iijima and co-workers reported a method to prepare densely packed and aligned CNTs using zipping effect as supercapacitor electrode material.[64] The specific capacitance of the aligned CNTs showed 80 F g^{-1}, which is roughly twice the value of 45 F g^{-1} for the entangled CNTs. Recently, Kim and co-worker have grown vertically aligned CNTs directly on conductive carbon papers using an Al/Fe catalyst *via* water-assisted CVD.[65] These aligned CNTs exhibited a specific capacitance of about 200 F g^{-1} at 20 A g^{-1}.

3.2 1D heterostructures

Unlike homostructures, heterostructures usually consist of more than one component. One major advantage of using heterostructured electrode design is the synergic improvement of intrinsic properties of each component for better electrical conductivity, faster ionic transport, greater electrochemical reversibility and cycle stability, and improved mechanical stability. Owing to these advantages, 1D heterostructures are currently considered as one of the potential candidates for the next generation electrode designs.

3.2.1 Core–shell 1D heterostructures. Core–shell 1D heterostructures often refer to a 1D nanostructure (*e.g.* nanorod, nanowire, nanotube, *etc*) coated with a thin shell. Among various heterostructures, core–shell heterostructures have received considerable attentions due to their unique structural properties that can effectively decline the surface energy which reduces the aggregation possibility of active materials as well as relieves side reaction between electrode and electrolyte, resulting in better reversibility and cycle stability of electrodes. Therefore, rational synthesis of advanced core–shell heterostructures with fascinating synergetic properties offers a promising approach to improve electrochemical performance. Typically, most of the core–shell heterostructures are prepared by initially creating a 1D nanostructured core backbone, followed by sheathing the shell materials. Various methods have been explored in order to obtain such advanced configuration including sputtering, electrochemical deposition, hydrothermal synthesis, CVD, electrospinning, *etc.* Due to the versatile combinations of electrode materials in terms of core and shell in a core–shell design, herein they are simply grouped into two categories: (1) current collector core – active material shell and (2) active material core – active material shell. For the convenience of discussion, we denote material A

(core) and material B (shell) as A@B for the remainder of the manuscript.

(1) Current collector core – active material shell. In this configuration, 1D nanostructured current collector core can provide shortened pathways for electron transport, which effectively enhances the available electrochemically active sites. Owing to the high electrical conductivity as well as excellent mechanical stability, metals have been selected as pivotal current collector candidates. When metals are forged into 1D nanostructures like nanowires or nanotubes, active materials can be deposited onto these 1D metal nanostructures and hence form core–shell 1D nanostructured electrode materials. There are several approaches to synthesize 1D metal nanostructures including template-assisted preparation,[66–69] soft solution processing,[49,70,71] vapor phase synthesis,[72–74] and self-assembling.[75,76] Among them, template-assisted preparation is the most intensively studied method for 1D metal nanostructure synthesis. Particularly, 1D metal nanostructures can be fulfilled by either shaping with the help of sacrificial templates (*e.g.* AAO) or directly coating active material on supercapacitive-inactive 1D nanostructures. For the former case, a pioneering work led by Teberna and co-workers reported Cu nanowire array prepared using AAO template as current collector, which was subsequently deposited with active materials (Fe_3O_4).[69] Following a similar concept, other works have been demonstrated such as Ni@MnO_2,[77,78] Ni@NiO,[79] Au@MnO_2,[80] Ni@Co_3O_4,[81] Mn@MnO_2,[82] *etc.* For the latter, since the inert core does not give any contribution to the electrochemical properties, the metal coated structure is still regarded as the current collector core.

There are several on-going efforts by Thomas's group to deposit metal on supercapacitive-inactive 1D nanostructures as current collector. Recently, they have demonstrated the synthesis of AuPd@MnO_2 core–shell structures for supercapacitor application.[52] AuPd was sputtered on PAN nanopillars prepared by SNAP technique, followed by electrochemical deposition of MnO_2 (Fig. 7a). Fig. 7b and c shows the SEM image of the as-printed structures, suggesting a highly ordered nanopillar structure. These nanopillars have diameter of ~140 nm, height of ~250 nm, and centre-to-centre distance of ~200 nm. As shown in Fig. 6d, MnO_2 were conformally coated onto each pillar. A modelling of the 3D surface area enhancement indicated a ~4.5 times surface area enhancement on the nanostructured region compared to a planar region (data based on the dimensions of nanopillars from SEM images). Accordingly, the specific capacitances of AuPd@MnO_2 core–shell nanopillars (603 F g^{-1}) consistently exhibited more than two-fold improvement compared to that of AuPd–MnO_2 planar electrode, at various scan rates.

Thomas and co-workers recently developed another strategy to prepare CuO@AuPd@MnO_2 core–shell nanowhiskers (NWs) as supercapacitor electrodes.[83] This was accomplished by sputtering AuPd on high aspect ratio CuO NWs (with diameter ~100 nm and length ~15 μm) that were obtained by simply

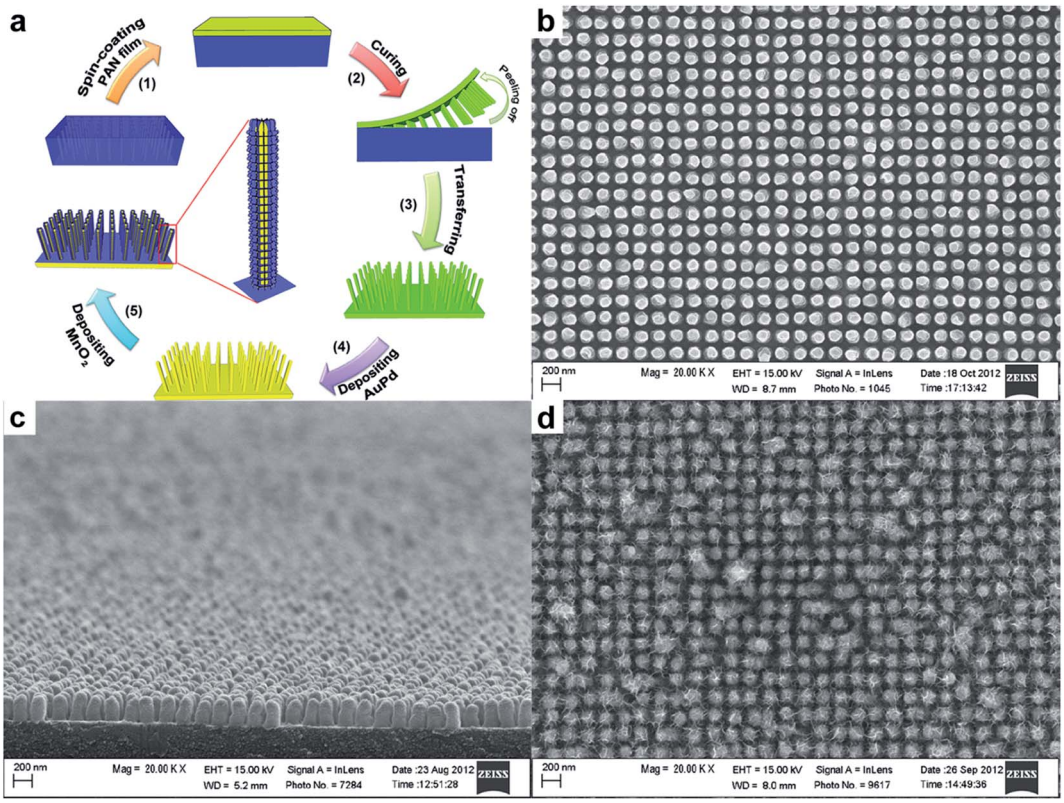

Fig. 7 (a) Schematic illustration of the development of MnO_2 coated electrodes. SEM images show top (a) and side (b) view of as-printed PAN nanostructures. (d) SEM image of electrochemically deposited MnO_2 nanoparticulates on pillar nanoarrays. Reproduced with permission from ref. 52. Copyright 2013 WILEY-VCH Verlag GmbH & Co. KGaA, Weinheim.

heating a copper substrate in air at elevated temperature. MnO_2 was then electrodeposited onto the CuO@AuPd structures hence producing CuO@AuPd@MnO_2 core–shell NWs. Fig. 8a shows the schematic illustration of the fabrication process of CuO@AuPd@MnO_2 core–shell NWs. Fig. 8b clearly presents that CuO NWs were grown uniformly on the Cu wire and Fig. 8c confirms that each CuO NW was conformally covered by MnO_2. The as-prepared core–shell heterostructures showed excellent specific capacitance of 1376 F g^{-1} at a scan rate of 5 mV s^{-1}. This may be attributed to two reasons: (1) the CuO nanowhiskers as scaffold provides substantially improved surface area (more than 2 orders of magnitude higher than a planar CuO substrate) for the electrode materials and (2) the core–shell heterostructures considerably enhance the ionic and electronic conductivity. Additionally, they have revealed that the CuO layer not only serves as high surface area scaffold but also works as an insulating layer to block charge transfer. As a result, they have successfully demonstrated that the inner copper wire can be used for electrical transmission as normal while an independent supercapacitor can be built on the outside by using overlapping layers. This led to the development of a dual-function (electrical conduction and energy storage) device.

In addition to metals, other materials such as ZnO, SnO_2, Zn_2SnO_4, and ITO have been fabricated into 1D nanostructures and served as current collector cores to deposit active material shells.[84–91] To date, most 1D current collectors are either nanowires or nanorods, while reports about nantubular current collectors are relatively few. However, electrodes based on nanotubular current collectors show promising results since both inner and outer surfaces can be utilized for depositing active materials.

(2) Active material core – active material shell. Active material core – active material shell presents another promising combination of 1D core–shell heterostructures since both core and shell materials contribute to electrochemical performance. Generally, active materials used in supercapacitors can be classified into two groups: EDLC materials and pseudocapacitive materials. There can be four types of core–shell combinations, namely, EDLC material core – EDLC material shell, EDLC material core – pseudocapacitive material shell, pseudocapacitive material core – EDLC material shell, and pseudocapacitive material core – pseudocapacitive material shell. Among these categories, EDLC material core – pseudocapacitive material shell and pseudocapacitive material core – pseudocapacitive material shells are the two major players.

EDLC material core and pseudocapacitive material shell constitutes an appealing combination of core–shell design due to the following merits: (1) EDLC materials as core have better cycle stability due to their electrostatic charge and discharge storage mechanism (*i.e.* no phase changes), which makes them robust backbones even for large number of cycles; (2) EDLC core material also have better electrical conductivity compared to pseudocapacitive materials, which facilitates the transportation of electrons; (3) pseudocapacitive materials as shell can effectively offset the low capacitance contribution from EDLC materials core. In this regard, Zhai and co-workers have demonstrated the feasibility of EDLC material core and pseudocapacitive material shell such as CNT@PPy–MnO_2,[92] CNT@PEDOT–MnO_2,[93] and CNT@PANI–MnO_2.[94] In CNT@PPy–MnO_2, multiwall CNTs were first well-dispersed and wrapped around using 18 wt% poly(4-styrenesulfonic acid) (PSS), which also provides attractive forces for pyrrole and metal ions upon negative charging. PPy–MnO_2 composite shell was subsequently prepared by adding pyrrole and $KMnO_4$ (Fig. 9). As a result, CNT@PPy–MnO_2 core–shell nanowires showed ~268 F g^{-1} specific capacitance, which is much higher than CNT@MnO_2 (~170 F g^{-1}) and CNT@PPy (~160 F g^{-1}). Significantly, 93%

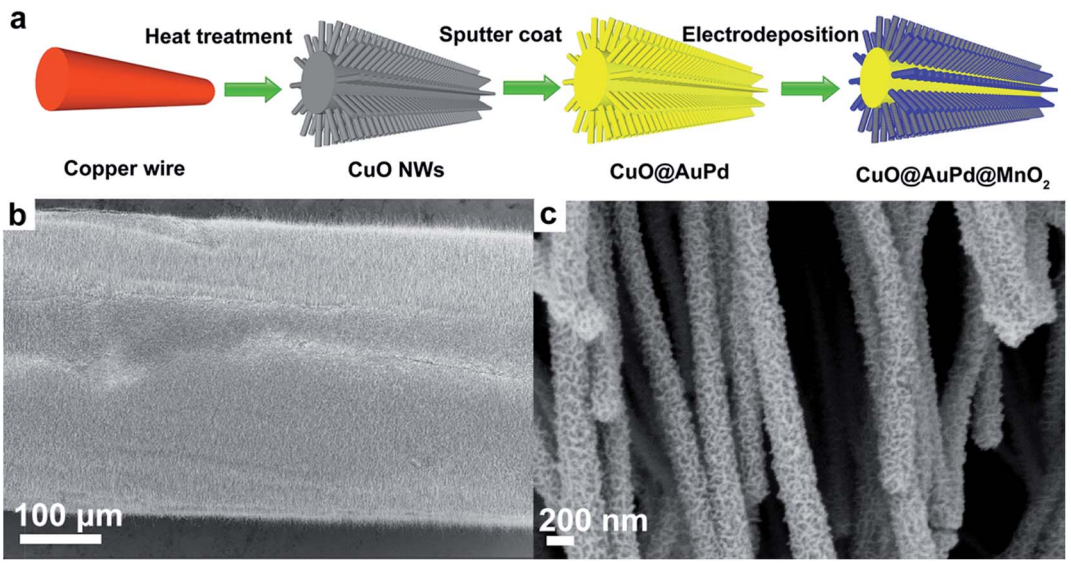

Fig. 8 (a) Schematic illustration of the fabrication process of CuO@AuPd@MnO_2 NWs. (b) SEM image shows that the copper wire is completely covered by CuO NWs. (c) SEM image of MnO_2 that was uniformly electrodeposited onto NWs. Reproduced with permission from ref. 83. Copyright 2014 WILEY-VCH Verlag GmbH & Co. KGaA, Weinheim.

rate capability of CNT@PPy–MnO_2 was retained from 5 to 100 mV s^{-1}, while only 35% and 72% were retained by CNT@MnO_2 and CNT@PPy respectively in the same scan rate range when tested separately. Moreover, CNT@PPy–MnO_2 exhibited very stable cycle life (10% reduction after 5000 cycles); in contrast, a specific capacitance reduction of 61% and 45% was observed under the same test conditions for CNT@MnO_2 and CNT@PPy, respectively.

A similar strategy reported by Ajayan and co-workers is the combination of CNT core and MnO_2 shell.[95,96] First, MnO_2 nanotubes were obtained by vacuum infiltrating manganese nitrate solution into an AAO template pre-electrodeposited with Au, followed by subsequent annealing in the air at 300 °C for 10 h. CNTs were then grown on the inner void left by the MnO_2 shells by CVD process and hence obtained CNT@MnO_2 1D core–shell heterostructure upon removing the AAO template. Significantly, the core–shell arrays showed almost two times enhancement of specific capacitance compared to pure MnO_2. Moreover, no apparent structural change was detected even after 1000 cycles, indicating remarkable mechanical and cycle stability.

Pseudocapacitive material core – pseudocapacitive material shell presents another intriguing core–shell design because both core and shell materials have redox reactions during charge and discharge processes, which results in high specific capacitances. In this regard, Fan's group has synthesized versatile combinations of pseudocapacitive materials with 1D core–shell heterostructures including Co_3O_4@MnO_2,[97] CoO@NiHON,[98] Co_3O_4@NiO,[99] CoO@TiO_2,[100] and Co_3O_4@PEDOT–MnO_2.[101] Taking Co_3O_4@MnO_2 core–shell nanowires as an example, Co_3O_4 nanowire core was first hydrothermally grown for 5 h, followed by coating a thin carbon layer and hydrothermal deposition of MnO_2 from a $KMnO_4$ solution at 160 °C for 1–5 h. The as-synthesized core–shell heterostructures presented a specific capacitance of 480 F g^{-1} at 2.67 A g^{-1} and excellent rate capability (56% retention with current density up to 44.7 mA cm^{-2}).[97] Following a similar concept, Liu and co-workers further improved the performance by employing $NiCo_2O_4$ instead of Co_3O_4 due to its better electronic conductivity (as mentioned earlier).[102] Consequently, the final product of $NiCo_2O_4$@$Ni_xCo_{1-x}(OH)_2$ core–shell nanowires considerably increased the specific capacitance up to 1500 F g^{-1} and improved the rate capability up to 67% retention at 90 mA cm^{-2}.

It should be noted that some of the metal oxides, such as V_2O_5, MnO_2 and Co_3O_4, suffer from dissolution issues due to phase changes upon cycling, which gradually erodes the quantity of electrochemically active materials, resulting in poor cycling and mechanical stability.[103–105] Therefore, a rational design like a durable protective coating which can effectively inhibit the structural collapse or break-down of metal oxide core and alleviate the strain generated during cycling is essential. In this regard, conducting polymers are generally selected as promising protective shell materials due to their high stability, mechanical flexibility, and excellent electronic conductivity.[106] For example, Wu and co-workers reported core–shell structure of PPy grown on V_2O_5 nanoribbon for supercapacitors.[103] V_2O_5 nanoribbons were first prepared hydrothermally in a solution containing NH_4VO_3 and poly(ethylene oxide)-*block*-poly-(propylene oxide)-*block*-poly(ethylene oxide) copolymer at 120 °C. The as-prepared V_2O_5 nanoribbons were dispersed in water by using anionic surfactant. The anionic surfactant also provided electrostatic force to absorb pyrrole at a later stage. After adding pyrrole and $FeCl_3$, a core–shell structured V_2O_5@PPy was obtained (Fig. 10a). Significantly, a supercapacitor assembled using V_2O_5@PPy as anode and activated carbon as cathode showed less than 5% capacitance fading after 10 000 cycles, while one assembled under the same condition without PPy film on the V_2O_5 anode showed 17.5% capacitance loss. This result demonstrates the effectiveness of PPy shell in preventing the dissolution of V_2O_5 upon cycling (Fig. 10b). Furthermore, the electrolyte for PPy@V_2O_5 electrode after cycling showed transparent color, while yellow electrolyte was observed for the V_2O_5 electrode, indicating that vanadium ions diffuse into the electrolyte without a protective coating. Similarly, other works employing conducting polymers as protective shell, including, MnO_2@PEDOT–PSS,[107,108] Co_3O_4@PANI,[109] MnO_2@PPy,[110,111] V_2O_5@PEDOT–MnO_2,[112] *etc.* have been

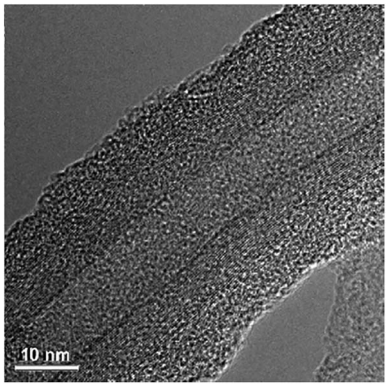

Fig. 9 High resolution TEM images of the MWCNT@PPy–MnO_2 core–shell structure. Reproduced with permission from ref. 92. Copyright 2009 Elsevier.

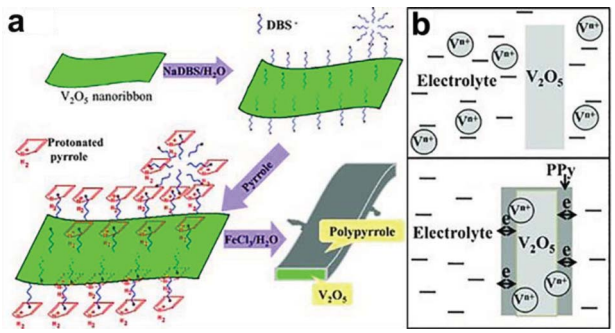

Fig. 10 (a) Schematic shows the growth of PPy on V_2O_5 nanoribbon surface. (b) PPy shell helps the electronic transport and prevents the dissolution of vanadium in electrolyte. Reproduced with permission from ref. 103. Copyright 2013 WILEY-VCH Verlag GmbH & Co. KGaA, Weinheim.

demonstrated. Further studies are needed to address the relationship between the thickness of protective coating and electrochemical performances (*e.g.* cycle stability and rate capability). This is because, even though the protective coating could effectively prevent the dissolution issue, it could, in turn, block the accessibility of ions if it is too thick, which impedes the rate capability.

3.2.2 Other 1D heterostructures. Composites containing 0D and 1D nanomaterials have been extensively studied for other heterostructures as well. For instance, by doping 0D nanomaterials into 1D nanomaterial matrix, Gu and co-workers have prepared vertically-aligned CNT arrays and doped them with MnO_2 nanoflowers by electrochemical deposition.[113] The MnO_2/CNT composites exhibited a specific capacitance of 199 F g^{-1} which is much higher than pristine CNT (27 F g^{-1}) and 97% capacitance retention even after 20 000 cycles. This impressive result may be attributed to the employment of CNT arrays, which provides not only high electronic and ionic conductivity but also sturdy mechanical stability. Another example reported by Lee and co-workers was the loading of well-dispersed MnO_2 nanoparticles into PEDOT nanowires.[114] PEDOT nanowires were first prepared by electrochemical deposition of PEDOT in AAO template, followed by removal of the template using NaOH solution. MnO_2 nanoparticles were subsequently loaded into the PEDOT nanowires by soaking the PEDOT nanowires into $KMnO_4$ solution. The MnO_2/PEDOT composites delivered a specific capacitance of 250 F g^{-1} and an 80% rate capability was maintained from 5 to 25 mA cm^{-2}.

4 2D nanostructures

Given the importance of properties such as diffusion ion length or contact area with electrolyte for utilization of active material in the performance of the electrochemical supercapacitors, the rise of 2D materials, and the fact that they exhibit only surface area (*i.e.* no bulk volume), has naturally attracted substantial interest and augmented a number of possible configurations of potential hybrid 2D configurations in the electrode material design. In addition, 2D materials exhibit unique properties such as mechanical stability, strength, flexibility, transparency, and chemical stability. However, in supercapacitors involving 2D structures, little is known of the unique behavior and properties most 2D materials and derived hybrid in aqueous or organic solvents that will exhibit. Since capacitance is highly dependent on the surface areas of the electrode materials, 2D materials are envisioned to bring a paradigm shift in the field of electrochemical capacitors.[115]

4.1 2D homostructures

The most widely explored materials for 2D homostructured-electrode fall under the following three categories. The first one includes graphene-based electrodes, which have been the most extensively investigated since its emergence, and found to have extensive applications in EDLC. Secondly, electrodes made of

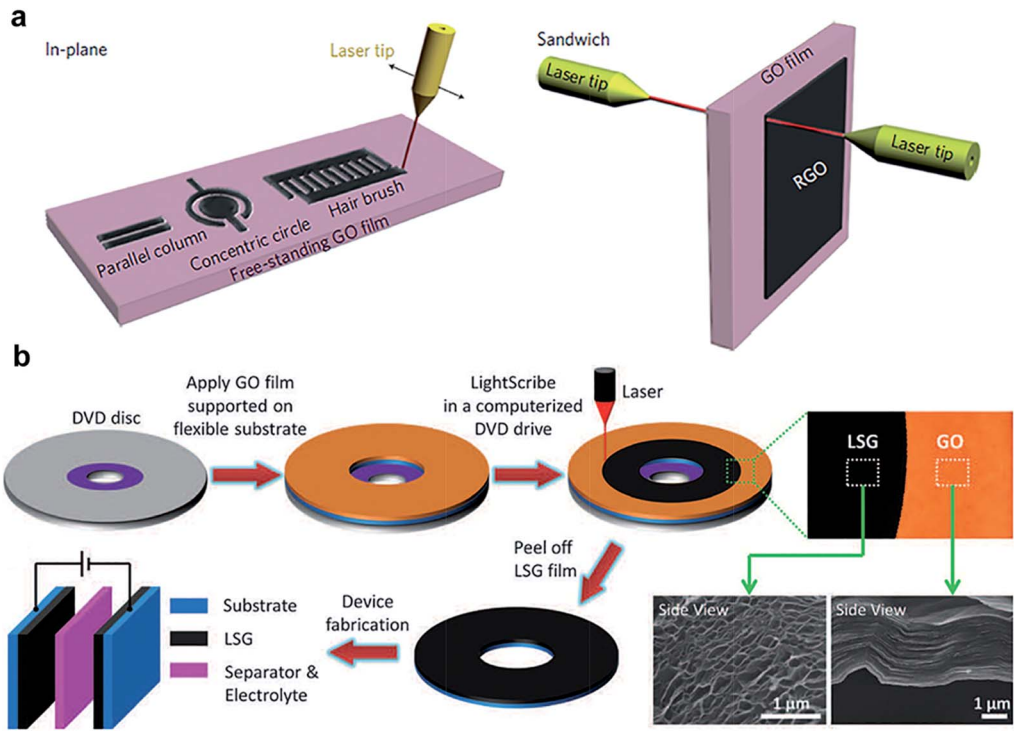

Fig. 11 (a) rGO–GO–rGO in-plane and sandwich devices obtained by laser patterning. (b) Laser-scribed graphene-based supercapacitors. Reproduced with permission from ref. 144 and 145. Copyright: 2011 Macmillan Publishers Limited and 2012 American Association for the Advancement of Science.

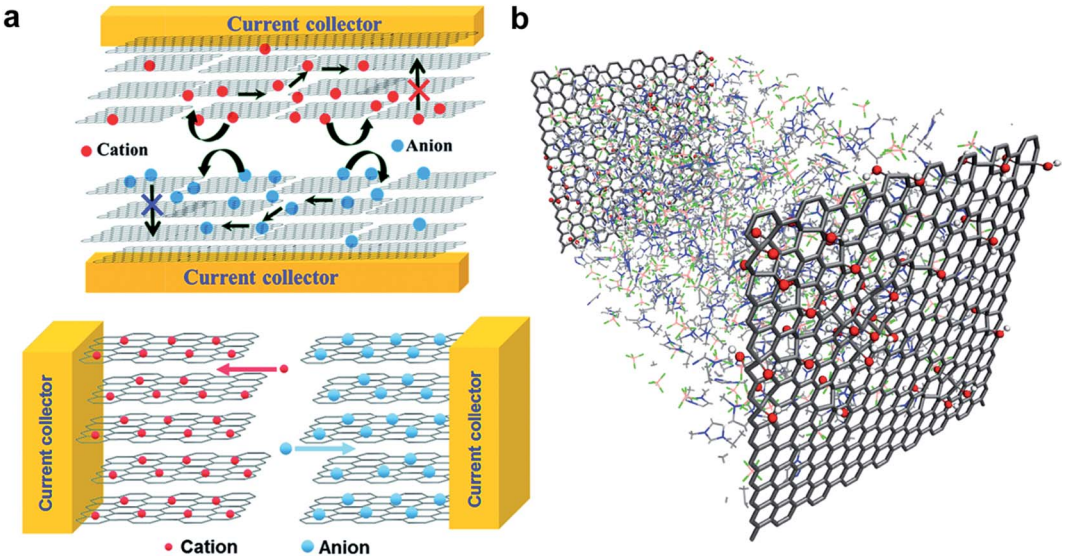

Fig. 12 (a) Conventional stacked geometry used for carbon based electrode material (top) and in-plane supercapacitor configuration made of graphene electrodes (bottom). The schematic depicts the mechanisms of increase in electrolyte percolation for higher performance. (b) Representation of a supercapacitor model consisting of GO electrodes (10% oxidation) with pure $EMI^{+}BF4^{-}$. Reproduced with permission from ref. 130 and 133. Copyright: 2011 and 2014 American Chemical Society.

metal oxides and hydroxides, which have also been widely studied as active materials for pseudocapacitors, will be discussed. Finally, recent developments in transition metal dichalcogenides (TMDs) including MoS_2 and VS_2 and transition metal carbides and/or nitrides (MXenes) will be overviewed.

4.1.1 Graphene. Various forms of carbon have been considered for electrode materials in supercapacitors.[116,117] Moderate specific capacitance together with long cycle life represent the holy-grail for carbon-based electrodes. Currently low conductivity of porous carbon material, despite their high surface area, constitutes a major limitation for supercapacitors with high-power density.[118,119] On the other hand, CNTs offer both high surface area and conductivity, but show high contact resistance at the electrode–current collector and expensive synthesis have hampered their scale up processing for large scale manufacturing. Thus, the emergence of graphene has provided an alternative to overcome the limitations of carbon-based electrodes and lead to new directions in the development and optimization of electrode materials. As a result, graphene is currently the most common material used for 2D material-based electrodes in energy storage devices due to its chemical stability (*i.e.* resistance to oxidative processes),[116,120–122] as well as its unique intrinsic electrical (*i.e.* fast transport of electrons), mechanical and thermal properties.[123] Recently, the capacitance of graphene in its monolayer form was experimentally measured ($\sim$21 μF cm^{-1}),[124] with a projected $\sim$500 F g^{-1} for an ideal single layer graphene-based EDLC, in which the surface area could be fully utilized. Such an electrode would constitute a record in carbon electrode materials for EDLCs but designing remains a great challenge.

In addition, as discussed by Ruoff and co-workers in one of the first demonstrations of graphene as electrodes for supercapacitors, it eliminates the necessity of using conductive fillers to improve the electrode conductivity.[125] It also offers the possibility to increase the electrode thickness while greatly improving the performance including a higher ratio of electrode material to collector/separator and higher energy densities. Moreover, large surface area of graphene is very attractive for supercapacitor electrode materials.[125–127] The surface area of graphene is predicted to be as high as 2630 m^2 g^{-1} and all the more exciting is the fact that it intrinsically consists of structured, accessible pores and interlayer spaces (*i.e.* better accessibility for ions).[125,126] Thin films of graphene electrodes have been obtained by various methods aiming at large scale production, including CVD,[128–130] electrostatic spray deposition,[129] electrophoretic deposition,[23,129] and ink-jet printing.[94,129,131] Nevertheless, to date, chemical approaches to make graphene oxide (GO) are the most cost-effective ton-scale method to produce graphene-based electrode materials. However, despite higher production yield, additional treatments are required to overcome its low conductivity. Among various treatments, chemically modified graphene (CMG) and reduced graphene oxide (rGO) are of particular interest as they offer a scalable and cost-effective chemical approach and produce a material with conductivity close to that of graphene.[116,125,132,133] As a result, rGO has been extensively used as a highly conductive electrode material and the mechanisms of reduction of GO becomes highly important in the development of 2D electrode materials for supercapacitors.

(a) Performance of chemically prepared rGO electrodes. A variety of reducing agents have been considered to restore the graphene network and its conductivity in the GO sheets.[134–137] Hydrazine is the most commonly reported reducing agent for GO reduction. Ruoff and co-workers described the synthesis of CMG by reduction of suspended graphene oxide in water using hydrazine hydrate.[125] The resulting sheets showed a surface area

of 705 $m^2 g^{-1}$ and provided specific capacitances of 135 and 99 F g^{-1}, respectively, in aqueous and organic electrolytes. Chen and co-workers discussed GO gas-based reduction by hydrazine at room temperature to lower agglomeration in the system.[116,117] The electrode materials resulting from their protocol were shown to surpass CMG or CNT-based supercapacitors,[125,138,139] with a maximum capacitance of about 205 F g^{-1}, energy density of 28.5 W h kg^{-1} in an aqueous electrolyte solution and ~90% specific capacitance retained after 1200 cycle tests. C–N and C–O bonds, creating numerous hydrophilic polar sites, were present in the material, and seemed to improve the wettability of the electrodes.[116] Despite the seemingly high packing of the layers, the agglomeration was shown to be lower than with other protocols, allowing ions from the electrolyte to penetrate in-between layers and increase the capacitance of the system.

Other reducing agents including hydroquinone[7,137] and NaBH4 [137,140,141] have also been used to reduce GO. Interestingly, activated graphene using KOH in GO, another form derived from graphene obtained by chemical activation of exfoliated GO prepared by Ruoff and co-workers, revealed large surface area (3100 $m^2 g^{-1}$), high specific capacitance (up to ~170 F g^{-1}) and great electrical conductivity.[132] Despite the chemical processes involved in the formation of the activated layers, low oxygen and hydrogen content were found in the final product. Furthermore, ~97% of the capacitance was retained after 10 000 cycles.

(b) Performance of rGO electrodes prepared by physical methods. Vacuum low-temperature exfoliation and laser treatments are among the physical methods used for the reduction of GO in energy storage applications. Chen and co-workers have recently demonstrated that graphene flakes obtained as a result of low-temperature vacuum exfoliation demonstrated excellent energy storage performance.[142] The devices were tested in aqueous and organic electrolytes and exhibited specific capacitance of 220 F g^{-1} and 120 F g^{-1}, respectively.[142]

Thermal treatment of GO suspension from 150–200 °C has also been shown to produce rGO by removing the oxygen from GO thus enabling high conductivity up to 5230 S m^{-1}.[137] A specific capacitance of 122 F g^{-1} at 5 mA could be achieved after thermal treatment at 200 °C, corresponding to a charge–discharge rate of ~1000 mA g^{-1}. This constitutes an improvement of the specific capacitance of ~20% by direct comparison with the performance of a supercapacitor prepared using rGO obtained with hydrazine,[125] and compares well with other standard electrode-materials.[143] The advantage of this approach is its potential for scalable "green" production of carbon-based supercapacitor electrode materials.

On the other hand, laser reduction of GO is also getting substantial attention,[144–147] in part due to the ability to pattern rGO–GO structures with customized geometries in the same piece of GO, in plane or in 3D. For example, Ajayan and co-workers have developed a laser writing technique to directly convert GO to rGO (Fig. 11a).[144] In their study, the structure of the laser induced rGO was found to be porous, due to the decomposition of functional groups and water during laser treatment. Due to the anisotropic nature of ion mobility and transport distances, the capacitance was found to be highly dependent on the geometry of the patterned structures. The highest area capacitance of 0.51 mF cm^{-2} was obtained for in-plane disc geometry with no electrolyte. Comparatively, an interdigitated rGO supercapacitor with an organic electrolyte and electrode of the same thickness exhibited a mean capacitance density of 0.4 mF cm^{-2}.[146] A 30 to 35% drop in capacitance was found after 10 000 cycles, but the same performance could be improved by long exposure to ambient environment or aqueous electrolytes.[144] In contrast, Kaner and co-workers found that the laser-treated GO obtained using a LightScribe CD/DVD optical drive can provide an impressive conductivity (~1740 S m^{-1}) (Fig. 11b).[145] In addition, the nanosheets were found to be well aligned, with outstanding mechanical properties (only 1% change in conductivity after 1000 bending cycles). The formation of rGO–GO interfaces by laser reduction paves the way to in-plane supercapacitors with new configuration of ion percolation for higher performance.

The laser reduction methods also addresses one of the several challenges that greatly impede the performance of the devices, in particular restacking of graphene nanosheets.[120] This phenomenon is caused by van der Waals interaction between successive graphene layers.[120] In fact this is one of many extensive research efforts that have been employed to develop protocols preventing graphene restacking. Curved graphene was also shown to improve the performance of supercapacitors by taking advantage of the maximum intrinsic surface capacitance and surface area.[127] In addition, the formation of rGO–GO interfaces by laser reduction paves the way to in-plane supercapacitors with new configuration of ion percolation for higher performance. As demonstrated by Ajayan and co-workers (Fig. 12a),[130] the in-plane design fosters ions to interact with all the graphene layers resulting in the maximum utilization of electrochemical surface area.

Given the diversity of the results obtained with GO and reduced GO, a fundamental model describing the electrode

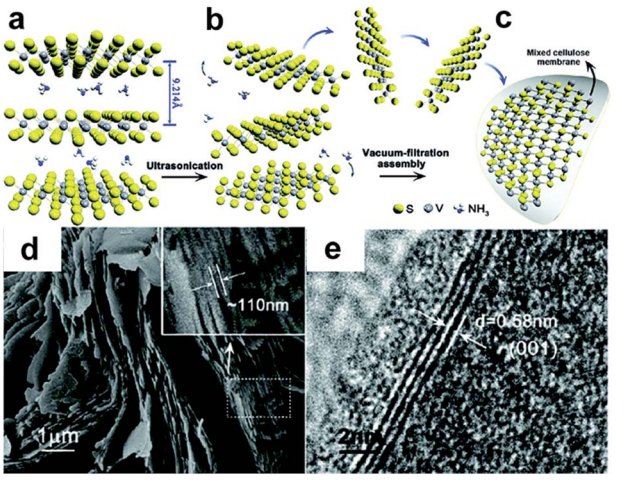

Fig. 13 VS_2 nanosheets for supercapacitor electrodes. S-V-S multilayers with intercalated NH_3 molecules (a) is used to exfoliate thin layers of VS_2 (b). The transfer is accomplished by vacuum filtration and the layers are transferred on mixed cellulose membranes (c). SEM (d) and HR-TEM (e) images of the multilayer with NH_3. Reproduced with permission from ref. 158. Copyright 2011 American Chemical Society.

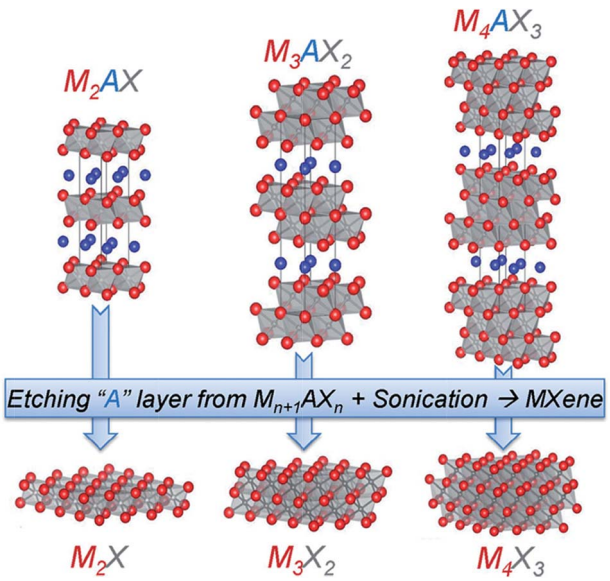

Fig. 14 Schematic of the fabrication of MXene. Reproduced with permission from ref. 162. Copyright 2013 WILEY-VCH Verlag GmbH & Co. KGaA, Weinheim.

polarizability, electrolyte dynamics, possible chemical processes, structural defects in the electrodes and pore characteristics would be of great interest to speed up the material discovery. However, this is a complex problem to model. Recently, Kim and co-workers considered the role of oxidation in molecular dynamics models (Fig. 12b) and demonstrated that the capacitance is highly dependent on the configuration of the oxidation,[133] as it modifies the electrode surface accessibility of the ions. Although limited in the parameters considered for the calculations, the approach shows great promise to catalyse electrode optimizations.

Overall, the initial reports of graphene-based electrodes in electrochemical supercapacitors indicated specific capacitance of 117 F g^{-1} in aqueous H_2SO_4 with operating voltage to 1 V for electrode preparation by graphitic oxide exfoliation and by nanodiamond transformation.[148] Specific capacitance of 135 F g^{-1} and voltage up to 1 V in aqueous media were obtained with CMG[125] with energy density of about 32 W h g^{-1}.[148]

4.1.2. Metal oxides and hydroxides. Metal oxides like RuO_2, IrO_2, MnO_2, NiO, Co_2O_3, SnO_2, V_2O_5 and MoO_2, are considered as important electrode materials for supercapacitors.[7] Their implementation in the form of 2D electrodes is taking the centre stage of hybrid device development. Deposition methods such as spin coating, anodization, electrodeposition, atomic layer deposition, spray deposition, and sputtering have been employed to deposit smooth thin films with optimal texture and low grain boundary density.[129,149]

2D MnO_2 (up to 2 nm in thickness) has been considered for cathode electrodes. Using soft template methods, Kang and co-workers showed high specific capacitance as high as 774 F g^{-1} up to 10 000 cycles.[150] The MnO_2 electrodes were used in aqueous $Ca(NO_3)_2$–SiO_2 gel electrolyte. The electrodes were prepared using a soft template technique. MnO_2 nanosheets were obtained by mixing sodium bis(2-ethylhexyl)sulfosuccinate and water to form a binary lamellar structure, to which $KMnO_4$ is added. The dissolution of $KMnO_4$ occurs only in the aqueous phase of the mixture and the growth of MnO_2 is automatically initiated in the aqueous phase. Scan rates from 2 to 50 mV s^{-1} could be demonstrated. For RuO_2 thin film electrodes, performances up to 730 F g^{-1} were demonstrated.[151,152]

4.1.3. Transition metal dichalcogenides (TMDs). Layered TMDS, in their monolayer forms, have recently taken an important role in material sciences for applications in opto-electronics, nanoelectronics and sensors. However, they have not been actively considered as possible electrode materials for supercapacitors. Although graphene in-plane design has

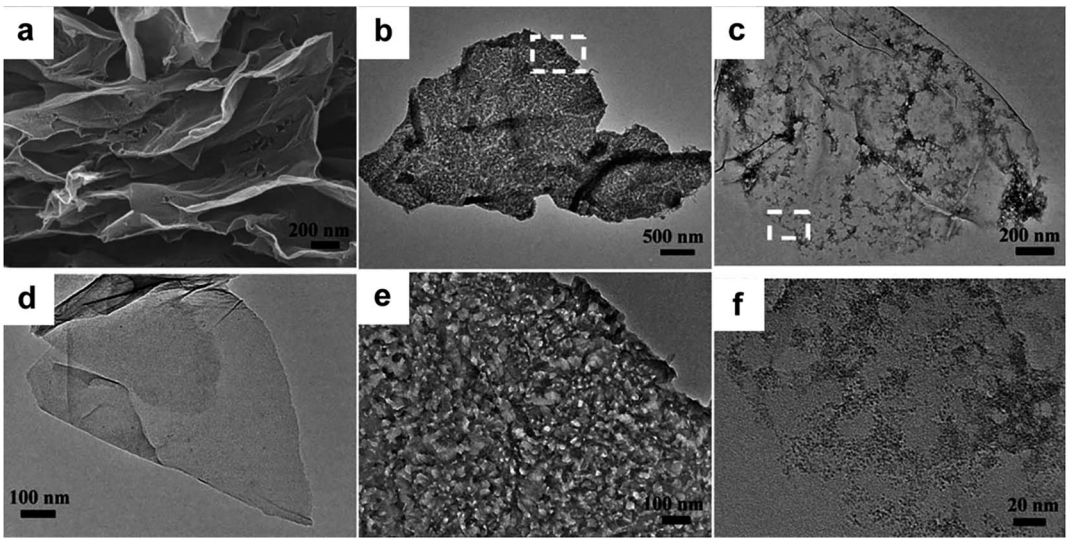

Fig. 15 (a) SEM images of rGO electrode materials. TEM image of rGO (b), rGO–PANi (c and d) and rGO–RuO_2 (e–f). Reproduced with permission from ref. 174. Copyright 2011 The Royal Society of Chemistry.

already demonstrated great results, its large scale implementation is hindered by high costs associated with the production of large-area low-defect sample. TMDs offer a variety of properties that could overcome the shortcomings of graphene. However, it remains to be seen whether TMDs may have an equivalent impact as graphene for in-plane supercapacitors.

Among TMDs being considered for electrode materials, MoS_2 may be of special interest for EC, as its intrinsic conductivity was calculated to be higher than other similar metal oxides, while its theoretical capacity was predicted to surpass that of graphite.[153,154] However, to date, the literature related to MoS_2 for EC electrodes is rather limited.[155,156] Soon and Loh carried out electrochemical impedance spectroscopy to characterize the performance of an arrangement of dense edge-oriented MoS_2 films for micro-supercapacitor and found that the performance is similar to that of CNT electrodes.[155,156] Other studies with various configuration of MoS_2 lead to medium performance electrodes.[102,111,157] More recently, flower-like MoS_2 electrode material developed by Geng and co-workers exhibited a specific capacitance of 168 F g^{-1} (at 1 A g^{-1}, 1 M KCl) and retained ~93% capacitance after 3000 cycles.[155]

Among other TMDs with intrinsically high conductivity, VS_2 represents a favorable alternative to graphene; further strengthened by the feasibility of exfoliation of layers after intercalation with NH_3 (Fig. 13).[158] Numerous tests were carried out on this new material. The conductivity remained constant throughout the 200 bending cycle test and is of great promise for flexible applications. The fabricated in plane device exhibited a specific capacitance ~317 F cm^{-3}, comparable to graphene based electrodes, with a good stability (90% after 1000 cycles).

4.1.4. Transition metal carbides and/or nitrides (MXenes). Recently, Gogotsi and co-workers introduced MXenes as a new family of promising 2D supercapacitor electrode materials.[159–162] MXenes consist of highly conductive carbide and carbonitride layers of which surfaces are designed to be hydrophilic and primarily hydroxyl-terminated. High capacitance (over 300 F cm^{-3}) can be achieved by cation (Mg^{2+}, K^+, Na^+, Al^{3+}, NH^{4+}, Ba^{2+}, Ca^{2+}, Cs^+, Li^+) intercalation, including those with various charges and sizes. Although ions intercalation is typically used in battery materials for energy storage, the slow diffusion rate hinder the charge–discharge performances. However, processes based on ion adsorption are often used in supercapacitors. In MXene, cation intercalation rates are unusually high, and the process is referred to as the intercalation pseudocapacitance.[163]

MXenes derive from the family of layered hexagonal MAX phases, a group including more than 60 forms of ternary nitrides or carbides, where M represents an early transition metal (*e.g.* Ti, V, Cr, Nb, *etc.*), A stands for an A-group element (*e.g.* Al, Si, Sn, In, *etc.*), and X represents C and/or N. The synthesis of MXene involves removing the A of MAX compounds by selective etching (Fig. 14). While numerous MXenes were predicted theoretically,[164,165] only about eleven MXenes are tested experimentally to date. Theoretically, it has been demonstrated that the surface termination (hydroxyl, fluorine) can be used to modify some of the MXene properties, such as their conductivity and bandgap.

Among the reported studies, a MXene, $Ti_3C_2T_x$, was obtained by etching Ti_3AlC_2 by hydrofluoric acid (HF) at room temperature.[161] A binder-free $Ti_3C_2T_x$ MXene material with surface area of 98 m^2 g^{-1} was obtained by delamination (single to few layers) and filtration of Ti_3AlC_2. It showed high flexibility and high volumetric capacitance (as high as 350 F cm^{-3}) in aqueous electrolyte NaOH.[159] To date, research towards electrode materials based on MXenes are limited; nevertheless, as a new promising 2D supercapacitor electrode material, much effort needs to be dedicated in this direction.

4.2 2D heterostructures

Regarding improvement of energy density in supercapacitors, making composites with transition–metal oxides and conducting polymers are being considered as they promise higher energy density than carbon materials. In addition, it has been shown that combining such high-energy metal oxides or conductive polymers with graphene based electrode materials can lead to high electrochemically accessible area. In addition, it leads to improvements in electrical conductivity, thermal stability and mechanical strength of the electrode, while minimizing the restacking of graphene layers.

4.2.1 Graphene–metal oxides and hydroxides. Graphene electrodes offer great potential for double layer capacitors. In addition, they were also found to be a versatile backbone to combine metal oxides nanostructures of known value for supercapacitors such as RuO_2, MnO_2, *etc.* Hybrids involving metal oxides offer great promise in the future of electrode materials as they can contribute to the total capacitance of the system by an added pseudocapacitance to the double layer capacitance from graphene[166,132] while the unique combination enable better chemical stability.[118] Increases in stability, capacity, rate performance and controlled crystallinity of the nanoscale structure of the active materials have previously been discussed.[121,167–171]

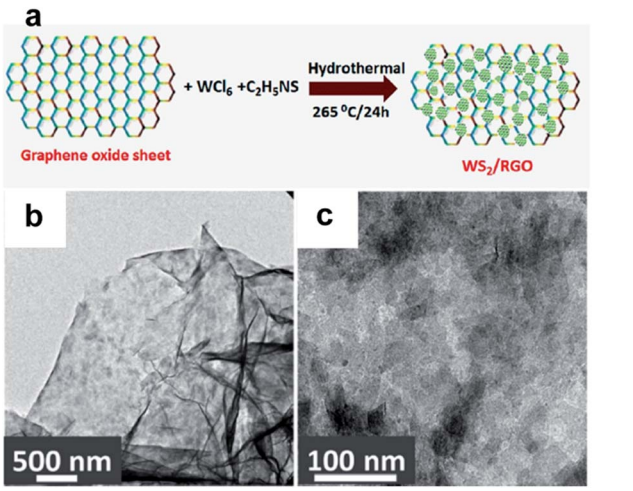

Fig. 16 (a) Hydrothermal synthesis of the WS_2–rGO materials. (b and c) TEM images of the resulting WS_2–rGO electrode material. Reproduced with permission from ref. 183. Copyright 2013 American Chemical Society.

As a very high conductivity metal oxide, RuO_2 has been known as a performing pseudocapacitive material.[104,121,172,173] Recently, Dai and co-workers synthesized a capacitor-like RuO_2–graphene (~30 wt% graphene sheets) hybrid in solutions,[121] which showed a specific capacitance of ~370 F g^{-1} (at 2 mV s^{-1}) and ~280 F g^{-1} at a scan rate of 40 mV s^{-1} in 1 M KOH solution for a 0.2 V to −1.0 V voltage range. Another investigation of the performance of RuO_2–rGO hybrid (Fig. 15) showed increasing capacitance with increasing Ru loading (at 16, 33 and 66 wt% Ru),[174] with a specific capacitance of 357 F g^{-1} at a current density of 0.3 A g^{-1}, which was attributed to the superior conductivity for rGO and an improved charge transport from RuO_2 to the rGO layers. This is supported by structural comparison to materials made of rGO (Fig. 15a and b), and rGO–PANI (Fig. 15c and d). $Ni(OH)_2$ nanoplates were also attached to graphene sheets to form a battery-like electrode material, and showed similar performance as RuO_2–graphene structures.[121] Finally pairing the two electrodes in an asymmetrical cell led to very attractive energy and power densities, suggesting that the performance of supercapacitors can be enhanced not only by hybrid electrode materials, but also by the combinations of electrodes with different properties.

Due to its great potential for enhanced supercapacitor performances, MnO_2 in combination with graphene has received substantial interest.[175–180] Wei and co-workers developed a facile method for graphene–MnO_2 hybrid electrode material by microwave irradiation.[179] With performance of 310 F g^{-1} at 2 mV s^{-1} (228 F g^{-1} at 500 mV s^{-1}), MnO_2–graphene surpasses pure graphene by a factor of three (104 and 103 F g^{-1}, respectively). About 95% of capacitance retention was observed even after 15 000 cycles. Another facile synthesis by Gao and co-workers showed high specific capacitance of 324 F g^{-1} in 1 M Na_2SO_4 with a retention of 97% after 1000 cycles.[177] Other metal oxides such as Fe_3O_4,[126] SnO_2,[181] and ZnO[166] are also mixed with graphene to make supercapacitor electrode materials.

4.2.2 Graphene-dichalcogenides. Although few attempts have been reported to add metal sulphides in the mix of electrode materials, their good electrochemical activity would suggest that they have great potential for energy storage devices.[182,183] Therefore, much effort needs to be dedicated towards this direction in the future.

MoS_2 has been combined with rGO to investigate the performance of hybrid energy storage devices. Covalent bonds occur between MoS_2 and the oxygen atom in RGO, forming a Mo–O–C bond. The resulting hybrid 2D material is electroactive, and could be cycled in 1 M $HClO_4$ between 0.25 V and up to 0.8 V, with energy density of 63 W h kg^{-1} and a specific capacitance decrease of 8% after 1000 cycles.[182]

WS_2–rGO hybrids, synthesised by a simple hydrothermal method, were evaluated for their performance as supercapacitor material (Fig. 16).[183] Comprehensive testing showed interesting specific capacitance of 350 F g^{-1} at a scan rate of 2 mV s^{-1} in 1 M Na_2SO_4, significantly higher than corresponding electrodes made of the bare materials measured at 130 and 70 F g^{-1}. In addition, a high energy density (~50 W h kg^{-1}) and the capacitance remained almost the same after 1000 cycles in the hybrid structure, due to the faster transport of electrolyte ions in the presence of WS_2.

4.2.3 Other hybrid configurations. Advances in device configurations and applications also require adjustment of the supercapacitor electrode materials. For instance, the implementation of 2D active materials in micro-supercapacitors faces new challenges due to the limited footprint of the device and subsequent loading mass limitations for the electrode. Therefore capacitance is highly limited in such devices, and calls for new electrode material configurations. To attain acceptable performance in such configuration, the emphasis is placed on high specific capacitance, conductivity and mechanical strength. Shen and co-workers used graphene and activated carbon as building blocks for thin electrodes made of an active material, a conductive agent and a polymer binder (carboxymethylcellulose sodium (CMC)).[184] Graphene served as the active material and the conductive agent. The graphene-based composite exhibited larger specific surface area and pore volume than the AC-based composite (surface area: 2156 *vs.* 1547 m^2 g^{-1}, pore size: 2.6 *vs.* 2.2 nm). In the 2D configuration, specific capacitance of ~60 mF cm^{-2} (100 μm thick electrode) was reported for the graphene-based electrode and up to ~310 mF cm^{-2} for activated carbon (200 μm thick electrode).

5 3D nanostructures

3D porous structures of active materials provide large surface area, well-defined pathways to electrolyte access and mechanical stability for efficient supercapacitor electrodes. Generally, 3D electrodes are built either using metal foam as templates or organizing active materials into 3D nanostructures.

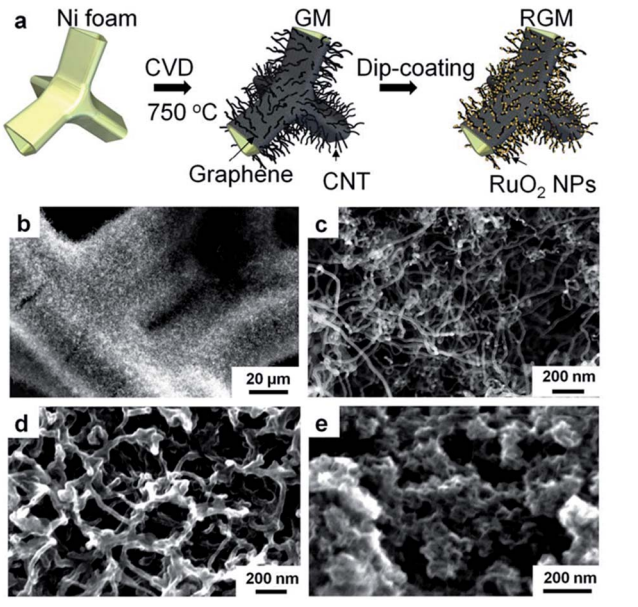

Fig. 17 (a) Schematic illustration of the preparation process of RGM nanostructure foam. SEM images of (b and c) as-grown GM foam, (d) lightly loaded RGM, and (e) heavily loaded RGM. Reproduced with permission from ref. 185. Copyright 2014 Macmillan Publishers Limited.

5.1 Metal foams as 3D nanostructured current collectors

Metal foams such as nickel foam provide highly porous and conductive substrates for the deposition of active materials including graphene, CNTs, conjugated polymers and metal oxides to build supercapacitor electrodes.[185–190] Compared with carbon based 3D substrates, metal foams have higher electrical conductivity and better mechanical properties but at the cost of larger density and lower specific surface area. 3D Co/Ni oxides with different morphologies were controllably synthesized and deposited on nickel foam substrates.[186] The synthesis involves a co-electrodeposition of bimetallic (Ni, Co) hydroxide precursors on a nickel foam scaffold and a subsequent thermal transformation of the precursors to Ni_xCo_{1-x} oxides. The crystal structure, morphology and electrochemical performance of the 3D Ni_xCo_{1-x} oxides can be readily manipulated by simply varying the Co/Ni molar ratio in the electrodeposition electrolyte. With the increase in the Co/Ni molar ratio, the structure changes from a NiO crystal dominant structure to $NiCo_2O_4$ and finally to a Co_3O_4 dominant structure. The unique 3D network architecture provides large solid/liquid interfacial area and facilitates efficient electron and ion transport. The electrode prepared with $Ni_{0.61}Co_{0.39}$ oxide on Nickel foam showed a specific capacitance of 1523.0 F g^{-1} at 2 A g^{-1} current density and retained 95.30% of its specific capacitance at a current density of 30 A g^{-1} after 1000 cycles. This electrode was used as a positive electrode with activated carbon as a negative electrode to build an asymmetrical supercapacitor and delivered a prominent energy density of 36.46 W h kg^{-1} at a power density of 142 W kg^{-1}.[186]

Ozkan and co-workers used nickel foams to grow graphene and CNTs followed by a deposition of ruthenium oxide (RuO_2) nanoparticles on CNTs (Fig. 17).[185] The hierarchical and porous structures enable efficient access of electrolyte to the active materials (CNT–RuO_2 network layer) and provide a conductive framework to charge transport attributed to the embedded CNTs. The composite had a high energy density of 39.28 W h kg^{-1} and power density of 128.01 kW kg^{-1} and showed an excellent cycle stability of 106% capacitance retention over 8100 cycles.

Similarly, electrodes were prepared using well-aligned CoO nanowire arrays grown on 3D nickel foams with polypyrrole uniformly immobilized onto nanowire surface to utilize high electrochemical activities of CoO and polypyrrole as well as the short ion diffusion pathway in ordered mesoporous nanowires.[190] Such synergy between materials and structures leads to a high specific capacitance of 2223 F g^{-1}, good rate capability, and good cycle stability (99.8% capacitance retention after 2000 cycles). An asymmetrical supercapacitor device fabricated using the hybrid materials as the positive electrode and activated carbon film as the negative electrode achieved a maximum voltage of 1.8 V, high energy density (~43.5 W h kg^{-1}) and power density (~5500 W kg^{-1} at 11.8 W h kg^{-1}), and outstanding cycle stability (~20 000 times with 91.5% capacitance retention).

Mn/MnO_2 core–shell 3D porous structures were fabricated from ordered polystyrene sphere templates. Mn was electrically deposited between polystyrene spheres from *N*-butyl-*N*-methyl pyrrolidinium TFSI ionic liquid solution of $MnCl_2$. After removing polystyrene template using tetrahydrofuran, the 3D Mn template was anodized in a KCl aqueous solution to produce a Mn/MnO_2 core–shell structure. Such core–shell

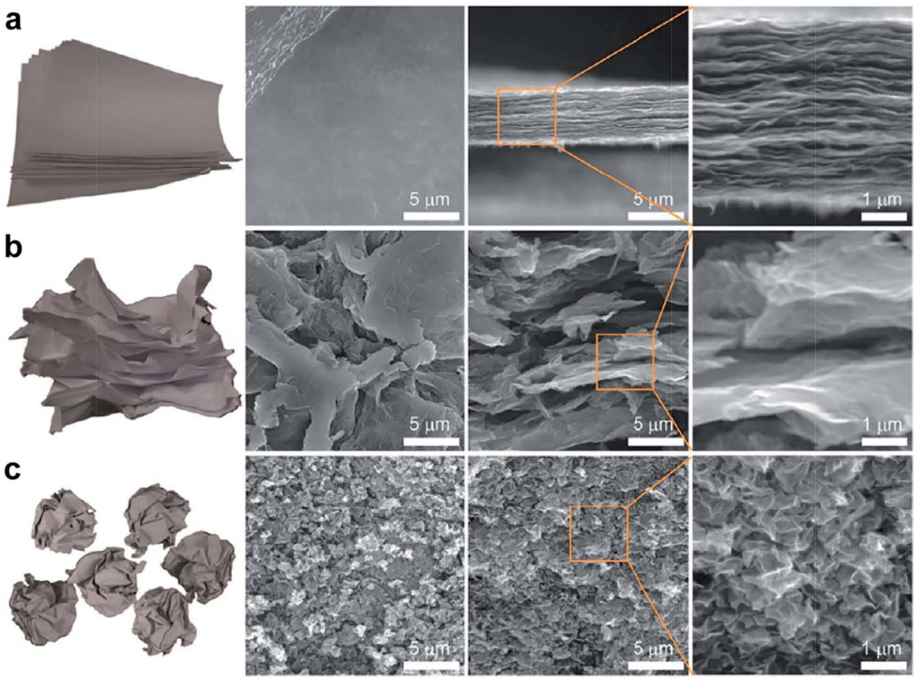

Fig. 18 Paper models and SEM images showing stacks of (a) flat graphene sheets, (b) heavily wrinkled sheets, and (c) crumpled graphene balls. Reproduced with permission from ref. 222. Copyright 2013 American Chemical Society.

porous structures contribute several positive factors including larger surface area, high electrical conductivity attributed to Mn and high capacitance of MnO_2 for efficient supercapacitors. Especially, the electrolyte can easily access the active material, leading to high specific capacitance at high scan rate. The optimum specific capacitance of the electrode at 500 mV s^{-1} is 996 F g^{-1}, maintaining 83% of the capacitance measured at 5 mV s^{-1}.[188] Composite supercapacitor electrodes based on metal foams have high electrical conductivity, good mechanical properties, and easy access of electrolyte to active materials, which leads to high specific capacitance and good cycle stability.

5.2 3D nanostructures based on carbon materials

Mesoporous carbon (MC) has been used as promising materials for supercapacitor electrode materials because of their large specific surface area and interconnected pores with tunable size. Since Ryoo and co-workers reported the fabrication of ordered MC from the ordered mesoporous silica molecular sieves as templates,[191,192] much effort has been devoted to exploring the application of such materials as supercapacitor electrodes. The studies of utilizing MC as electrode materials for EDLCs suggest that the pore size and symmetry have profound effect on the performance by influencing the accessibility of electrolytes. The pore size distribution with best performance ranges from 0.6 to 3 nm depending on different types of electrolytes.[193,194] While these EDLCs can reach the specific capacitance of 140 F g^{-1} which is much higher than those using commercial carbon, their performance is limited by the relatively low electrical conductivity.[195]

Further improvement can be achieved by doping[196] and depositing electrochemically pseudocapacitive materials such as metal oxides,[197–199] PANI,[200–204] and their mixtures[205] onto MC templates. For example, nitrogen- and sulfur-codoped 3D cubic ordered MC (KNOMC) materials with controlled dopant content (10.0–4.6 atom % for nitrogen and 0.94–0.75 atom % for sulfur) have demonstrated a specific capacitance of 320 F g^{-1} because the incorporated S and N species function as pseudo-active materials.[196] Metal oxides have also been added onto MC to increase the capacitance. For example, MnO_2 nanoparticles were imbedded in the MC through a redox reaction between permanganate ions and carbons.[199] The ordered mesoporous structures were retained through the control of the concentration of permanganate ion. The resulted composite structure showed a specific capacitance of 200 F g^{-1} with decent electrochemical stability and reversibility. Nanostructured PANI has been deposited on various MC substrates through chemical oxidative polymerization and it greatly increased the specific capacitance due to its high capacitance and electrical conductivity.[206] Li and co-workers have deposited PANI needle-like structures on MC and studied the effect of the structure on electrochemical properties.[202] It was found that the composite with 60% PANI deposition has the best performance (517 F g^{-1}), suggesting that a bimodal pore structure with some open pores facilitates the ion diffusion and shorten the charge transfer distance. PANI–CMK-3–MnO_2 ternary nanocomposites were built by co-deposition of conductive PANI and MnO_2 on MC and further improved the specific capacitance to 695 F g^{-1}.[205] In such composite, MnO_2 nanoparticles stabilizes the interaction between the quinoid ring of PANI and the CMK-3–MnO_2, while the PANI nanolayer retards the dissolution of MnO_2 nanoparticles during the charge–discharge process, leading to high cycle stability.

Theoretical studies[207,208] and experimental investigation[209] of the effect of pore size and distribution on ionic transport properties of porous structures suggest that the coexistence of macropore and mesopore would increase the efficiency of porous carbon as supercapacitor electrodes. Compared with MC, an ordered carbon structure with meso/macro/micropores can achieve a specific capacitance as high as 350 F g^{-1}.[209] Hierarchical carbon structures with a combination of meso/macro/micropores have been produced through various approaches,[210–218] and used as electrode with and without metal oxides.[219,220] These structures have demonstrated great potential in constructing high performance supercapacitors. Further improvement requires better control of pore size and distribution as well as increased electrical conductivity of porous carbon.

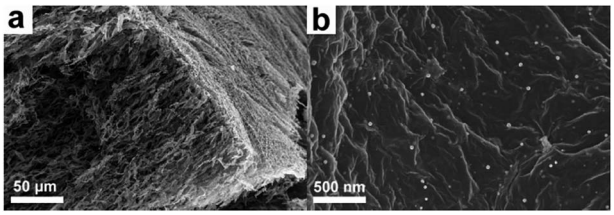

Fig. 19 SEM images of (a) functionalized graphene aerogel and (b) graphene nanosheets uniformly loaded with metal nanoparticles.

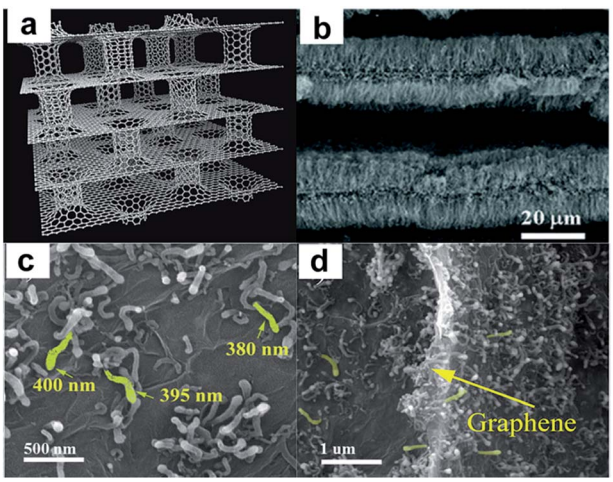

Fig. 20 (a) Schematic diagram of a 3D pillared VACNT–graphene nanostructure. (b) A SEM image of the thermally expanded graphene layers intercalated with VACNTs for 10 minutes pyrolysis times. (c and d) SEM images of CNTs grown on graphene using urea as carbon sources. Reproduced with permission from ref. 240–242. Copyright: 2008, 2011, and 2014 American Chemical Society.

Taking advantages of extraordinary properties of CNTs and graphene including large specific surface area, high electrical conductivity and superior strength, assembling CNTs and graphene into 3D porous structures offers excellent opportunities for building high performance supercapacitors. 3D CNTs and graphene not only provide large surface area for double layer supercapacitors but also function as supports for metal oxides and conjugated polymers for pseudocapacitors. GO sheets dispersed in aqueous solutions offer promising materials for building 3D structures for graphene based supercapacitors. The GO can be reduced chemically or thermally to increase the electrical conductivity. To eliminate the aggregation of graphene sheets that limits the electron and ion transport, Huang and co-workers have transformed 2D graphene sheets into crumpled paper ball structures by isotropic capillary compression in rapidly evaporating droplets of GO dispersion using an aerosol spray pyrolysis setup.[221] Fig. 18 compares the microstructures of mechanically compressed pellets of stacked graphene materials of flat graphene sheets (a), heavily winkled sheets (b) and crumpled graphene balls (c) using surface and cross sectional SEM.[222] The flat graphene sheets pack like a stack of paper with a smooth featureless surface and an ordered lamellar cross section (Fig. 18a). The pellets of wrinkled sheets (Fig. 18b) have uneven surfaces with many flattened islands in micrometers. The cross sectional SEM indicates a largely lamellar but significantly more disordered microstructure. For the crumpled balls (Fig. 18c), the morphology of individual particles in the compressed pellet was largely unchanged. Compared to flat or wrinkled sheets, the crumpled graphene balls have larger surface area and better defined voids for electron and ion transport. The electrodes based on crumpled graphene balls can deliver much higher specific capacitance (150 F g^{-1}) and better rate capability. Furthermore, using flat graphene sheets as binder for the crumpled particles eliminates the use of insulating binder materials like PTFE colloids and further improve device performances.[222]

Graphene aerogel (GA) as electrode material for supercapacitor has drawn considerable attention lately due to its open 3D network structure that not only effectively reduces the aggregation of graphene nanosheets but also facilitates effective electrolyte ion transportation. As a result, more electrochemically active sites could be utilized compared to 2D graphene nanosheets. For example, Duan and co-workers have prepared a 3D holey graphene framework with a hierarchical porous structure by etching the GO sheets *via* H_2O_2 molecules.[223] The resulting holey graphene framework showed a large specific surface area of 830 m^2 g^{-1}, which is significantly greater than that of non-holey one (~260 m^2 g^{-1}). As a consequence, holey graphene framework electrodes delivered a specific capacitance of 310 F g^{-1} at 1 A g^{-1}, while 208 F g^{-1} was achieved for non-holey graphene framework electrodes. It is to be noted that the electrical conductivity of GA is generally lower than that of pristine graphene due to the formation of defect sites during the oxidation–reduction process.[224] It is advantageous to fabricate a GA with enhanced electrical conductivity. Recently, Thomas, Zhai, and co-workers have reported functionalized GA composites as supercapacitor electrodes with reduced electrical resistivity by incorporating palladium nanoparticles (Fig. 19a and b).[225] The electrical resistivity of the functionalized GA (16 Ω cm) is substantially reduced compared to pristine GA (950 Ω cm). Consequently, the specific capacitance of the functionalized GA reached 175.8 F g^{-1}, while only 51.9 F g^{-1} was obtained for the pristine GA.

Similar to MC, high performance composite electrodes have been developed by doping graphene with nitrogen and boron[226] and integrating pseudo-active materials on 3D CNT and graphene structures.[227–239] 3D macroporous electrodes of chemically modified graphene (CMG) were fabricated using polystyrene colloidal particles as a sacrificial template.[227] A thin layer of MnO_2 was deposited onto the porous electrodes to further improve the capacitance. The porous graphene structure facilitates fast ionic transport within the electrode while preserving decent electrical conductivity. Such combination grants the electrodes excellent electrochemical properties such as high specific capacitance (389 F g^{-1} at 1 A g^{-1}) and 97.7% capacitance retention when the current increases to 35 A g^{-1}. In addition, an asymmetrical supercapacitor assembled using MnO_2/CMG composite electrode and a CMG electrode achieves an energy density of 44 W h kg^{-1}, a power density of 25 kW kg^{-1}, and excellent cycle life.

As discussed previously, ordered 3D porous structures with controlled pore size and distribution would improve the electrochemical properties. The concept of inherently nanoporous 3D pillared vertically aligned carbon nanotube (VA-CNT)–graphene hybrid architecture with a large surface area has been

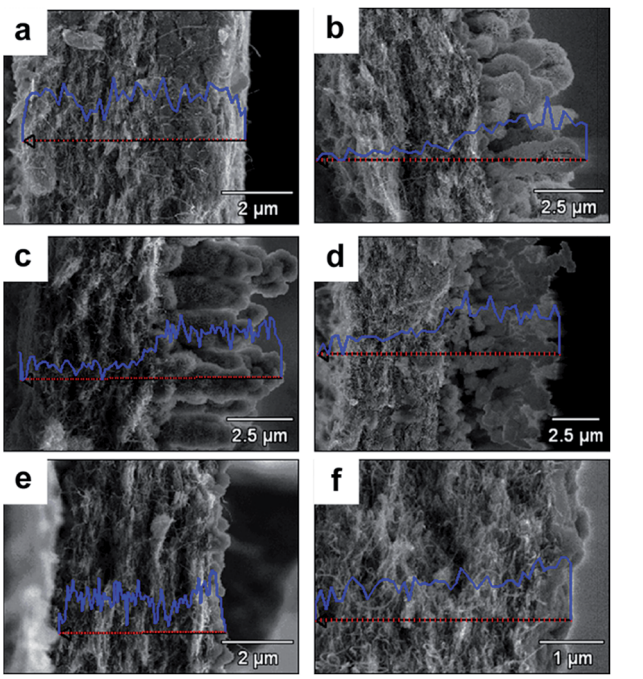

Fig. 21 Cross-section morphologies and X-ray line scan spectra of Mn element in pristine composites (MCM0), and after 500 cycles at 20 mV s^{-1} (MCM20), 60 mV s^{-1} (MCM60), 100 mV s^{-1} (MCM100), 300 mV s^{-1} (MCM300), and 500 mV s^{-1} (MCM500). (a) MCM0, (b) MCM20, (c) MCM 60, (d) MCM100, (e) MCM300, and (f) MCM500. Reproduced with permission from ref. 232. Copyright 2012 Elsevier.

explored to develop efficient supercapacitors (Fig. 20a).[240–242] Dai and co-workers prepared a VA-CNT–graphene hybrid by the intercalated growth of VA-CNTs into thermally expanded highly ordered pyrolytic graphite (Fig. 20b).[241] The resulting VA-CNT–graphene hybridized with a nickel hydroxide coating also demonstrated a high specific capacitance with a notable charging-rate capability, as high as 1065 F g^{-1} (based on the active material) at a current density of 22.1 A g^{-1}. Sun and co-worker have grown carbon nanotubes on graphene sheets through a facile one-pot pyrolysis strategy where cobalt ions and urea were mixed with GO followed by drying and heating the mixture at 900 °C. The length of the carbon nanotubes was tuned by adjusting the amount of precursors (Fig. 20c and d). The resulting graphene–CNT composites showed a high specific surface area of 903 m^2 g^{-1} and maximum specific capacitance of 413 F g^{-1}.[242]

As an example of depositing pseudocapacitive metal oxides on graphene/CNT scaffolds, 3D flower-like β-$Ni(OH)_2$/GO/CNTs composites were prepared *via* a facile hydrothermal reaction in alkaline solutions. CNTs were introduced to the composite to improve the electrical conductivity. The electrochemical properties of the composites produced at different reaction time were evaluated to understand the effect of composite structures on energy storage efficiency. Hydrothermal reaction converted α-$Ni(OH)_2$ to β-$Ni(OH)_2$ (1 h reaction time) and further 3D β-$Ni(OH)_2$ nanoflowers to stacked nanosheets (10 h). The electrochemical characterization of three different structures indicates that β-$Ni(OH)_2$ composite prepared through one hour hydrothermal reaction has the best performance with a high specific capacitance of ~1815 F g^{-1} based on $Ni(OH)_2$ (nearly 96% of its theoretical pseudocapacitance) at 2 A g^{-1} and a good cycling performance of ~97% capacitance retention after 2000 cycles at 10 A g^{-1}, attributed to higher stability (*vs.* α-$Ni(OH)_2$) and more efficient ion diffusion (*vs.* stacked β-$Ni(OH)_2$).[228]

Zhai and co-workers have incorporated MnO_2 into MWCNT 3D networks as supercapacitor electrodes. More importantly, they have discovered the relationship between MnO_2 migration phenomenon and the scan rates. The structural evolution were examined by studying the structure and electrochemical properties of identical electrodes after 500 CV cycles at various scan rates.[243] By using Electrochemical Quartz Crystal Microbalance (EQCM) to monitor the mass change of the electrode *in situ* and SEM to examine the electrodes after CV cycles, MnO_2 was found to "migrate" from the MWCNTs network and "deposit" on the electrode surface upon cycling. The structural change mechanism contains the dissolution of MnO_2 upon reduction, the diffusion of the reduced Mn species from the MWCNT network toward the electrolyte solution, and the deposition of MnO_2 on the electrode surface upon oxidation.[243] The structural change of MnO_2 is highly dependent on the scan rate. For instance, the reduced Mn species have more diffusion time at a lower scan rate, while less reduced species are generated due to the lower associated current density and *vice versa*. A scan rate that might cause the greatest structural evolution of MnO_2 is expected based on this contradictory effect. Fig. 21a shows the cross section of as-synthesized MWCNT/MnO_2 composites sprayed on a graphite substrate (MCM0) as well as an X-ray line scan

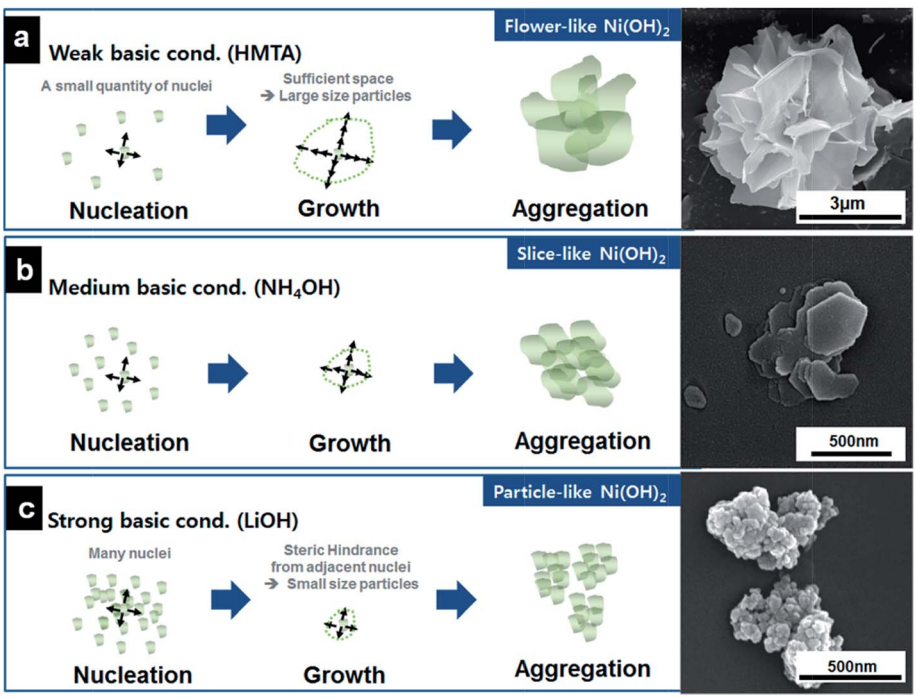

Fig. 22 Schematic diagram showing the formation process of (a) flower-, (b) slice-, and (c) particle-like $Ni(OH)_2$ under different pH conditions; corresponding SEM Images of as-prepared samples are in the Right Panel. Reproduced with permission from ref. 244. Copyright 2013 American Chemical Society.

Table 1 Properties and characteristics of supercapacitors electrode materials based on various dimensional nanostructures

Category	Subcategory	Selected examples	Electrochemical properties	Ref.
0D	0D solid nanostructures	Onion-like carbon	0.9 mF cm^{-2}; ~70% rate capability from 1 to 100 V s^{-1}; ~100% capacitance retention after 10 000 cycles	23
		Porous Au/MnO_2 hybrid electrode	1145 F g^{-1} at 50 mV s^{-1}; 80% capacitance retention after 500 cycles	24
		$LaMnO_3$ perovskite nanoparticles	609.8 F g^{-1} at 2 mv s^{-1}; 57% rate capability from 2 to 100 mV s^{-1}	25
	0D hollow nanostructures	Hollow carbon nanospheres	251 F g^{-1} at 50 mV s^{-1}; 77% rate capability from 50 to 500 mV s^{-1}; 98% capacitance retention after 200 cycles	28
		NiO multi shelled nanospheres	612.5 F g^{-1} at 0.5 A g^{-1}; 83.1% rate capability from 0.5 to 3 A g^{-1}; 90.1% capacitance retention after 1000 cycles	34
	0D core–shell nanostructures	HCS@PANI core–shell spheres	525 F g^{-1} at 0.1 A g^{-1}; 50% rate capability from 0.1 to 10 A g^{-1}; 73% capacitance retention after 1000 cycles	37
		GHCS@MnO_2 core–shell spheres	190 F g^{-1} at 0.1 A g^{-1}; 55% rate capability from 0.1 to 10 A g^{-1}; 99% capacitance retention after 1000 cycles	38
1D	1D homostructures	Oxygen-deficient Fe_2O_3 nanorods	64.5 F g^{-1} at 10 mV s^{-1}; ~35% rate capability from 10 to 400 mV s^{-1}; 95.2% capacitance retention after 10 000 cycles	50
		Carbon nanopillars	3.4 mF cm^{-2} at 100 mV s^{-1}; 95% capacitance retention after 10 000 cycles	51
		PANI nanowires	1142 F g^{-1} at 5 A g^{-1}; 82% rate capability from 1 to 40 A g^{-1}; 95% capacitance retention after 500 cycles	55
		$NiCo_2O_4$ nanoneedle arrays	1118.6 F g^{-1}; 89.4% capacitance retention after 2000 cycles	59
		MnO_2 nanotube arrays	320 F g^{-1} at 20 mV s^{-1}; 70% rate capability from 1 to 10 A g^{-1}; 81% capacitance retention after 2000 cycles	60
		Vertically aligned CNTs	200 F g^{-1} at 20 A g^{-1}; 72% rate capability from 20 to 150 A g^{-1}	65
	1D heterostructures	AuPd@MnO_2 core–shell nanopillars	603 F g^{-1} at 5 mV s^{-1}; 52% rate capability from 5 to 100 mV s^{-1}; 93% capacitance retention after 5000 cycles	52
		CuO@AuPd@MnO_2 core–shell nanowhiskers	1376 F g^{-1} at 5 mV s^{-1}; 58% rate capability from 5 to 100 mV s^{-1}; 99% capacitance retention after 5000 cycles	83
		CNT@PPy–MnO_2 core–shell nanotubes	268 F g^{-1}; 93% rate capability from 5 to 100 mV s^{-1}; 90% capacitance retention after 5000 cycles	92

Table 1 (*Contd.*)

Category	Subcategory	Selected examples	Electrochemical properties	Ref.
		Co_3O_4@MnO_2 core–shell nanowires	480 F g^{-1} at 2.67 A g^{-1}; 56% rate capability from 4 to 44.7 mA cm^{-2}; 97.3% capacitance retention after 5000 cycles	97
		V_2O_5@PPy core–shell nanoribbons	308 F g^{-1} at 100 mA g^{-1}; 95% capacitance retention after 10 000 cycles	103
2D	2D homostructures	Chemically modified graphene (CMG)	135 F g^{-1} at 10 mA; 97% rate capability from 20 to 400 mV s^{-1}	125
		Laser reduced graphite oxide	0.51 mF cm^{-2} at 40 mV s^{-1}; 70% capacitance retention after 10 000 cycles	144
		2D MnO_2	774 F g^{-1} at 0.1 A g^{-1}; 63% rate capability from 0.1 to 1 A g^{-1}; >100% capacitance retention after 10 000 cycles	150
		Flower-like MoS_2 nanosheets	168 F g^{-1} at 1 A g^{-1}; 92.6% capacitance retention after 3000 cycles	155
		VS_2 nanosheets	317 F cm^{-3}; ~100% capacitance retention after 1000 cycles	158
		$Ti_3C_2T_x$ (MXene)	350 F cm^{-3} at 1 A g^{-1}; ~60% rate capability from 2 to 100 mV s^{-1}; ~100% capacitance retention after 10 000 cycles	159
	2D heterostructures	RuO_2–graphene hybrid	~370 F g^{-1} at 2 mV s^{-1}; 76.3% rate capability from 2 to 40 mV s^{-1}; 92% capacitance retention after 5000 cycles	121
		Graphene–MnO_2	310 F g^{-1} at 2 mV s^{-1}; 73.5% rate capability from 2 to 500 mV s^{-1}; 95% capacitance retention after 15 000 cycles	179
		MoS_2–rGO	265 F g^{-1} at 10 mV s^{-1}; 77.4% rate capability from 10 to 80 mV s^{-1}; 92% capacitance retention after 1000 cycles	182
		WS_2–rGO	350 F g^{-1} at 2 mV s^{-1}; 42.8% rate capability from 2 to 200 mV s^{-1}; ~100% capacitance retention after 1000 cycles	183
3D	3D metal foam	$Ni_{0.61}Co_{0.39}$ oxide on nickel foam	1523.0 F g^{-1} at 2 A g^{-1}; 95.3% capacitance retention after 1000 cycles	186
		CoO–PPy on 3D nickel foam	2223 F g^{-1} at 1 mA cm^{-2}; 29.1% rate capability from 1 to 50 mA cm^{-2}; 99.8% capacitance retention after 2000 cycles	190
		Mn/MnO_2 core–shell 3D porous structure	~1200 F g^{-1} at 5 mV s^{-1}; 83% rate capability from 5 to 500 mV s^{-1}; 96% capacitance retention after 2000 cycles	188

Table 1 (*Contd.*)

Category	Subcategory	Selected examples	Electrochemical properties	Ref.
	3D carbonaceous materials	Crumpled graphene balls	150 F g^{-1} at 0.1 A g^{-1}; 40% rate capability from 0.1 to 2.5 A g^{-1}; ~100% capacitance retention after 5000 cycles	222
		VA-CNT–graphene with $Ni(OH)_2$ coating	1065 F g^{-1} at 22.1 A g^{-1}; 70% rate capability from 5 to 30 mV s^{-1}; 96% capacitance retention after 20 000 cycles	241
		β-$Ni(OH)_2$/GO/CNTs	1815 F g^{-1} at 2 A g^{-1}; 47.2% rate capability from 2 to 20 A g^{-1}; 97% capacitance retention after 2000 cycles	228
	3D pseudocapacitive materials	3D NiO nanoflowers	480 F g^{-1} at 0.5 A g^{-1}; 52.5% rate capability from 0.5 to 5 A g^{-1}; ~90% capacitance retention after 400 cycles	244
		3D Co_3O_4 urchin-like nanostructures	781 F g^{-1} at 0.5 A g^{-1}; 78.2% rate capability from 0.5 to 8 A g^{-1}; 97.8% capacitance retention after 1000 cycles	245

spectra of Mn element. The SEM and X-ray line scan spectral data clearly exhibit that MnO_2 nanoflakes are uniformly embedded in the MWCNTs network as the active materials while the MWCNT network serves both as the support for MnO_2 nanoflakes and current collector. In contrast, Fig. 21b–f shows the striking changes of electrode structures after 500 CV cycles, and the structural change varies at different scan rates. As a result, a higher specific capacitance could be achieved with a lower scan rate; however, the specific capacitance considerably drops upon cycling due to the dissolution of active material. Therefore, either developing a protective layer as mentioned in the 1D section or manipulating a suitable scan rate that induces the least structural changes while maintaining high specific capacitance is required.

5.3 3D nanostructures based on pseudocapacitive materials

Different nanostructures of pseudocapacitive materials offer intriguing composition for 3D supercapacitors. Various types of metal oxide nanostructures produced through sol–gel, solvothermal and other approaches have been evaluated electrochemically to understand the impact of their structures on the energy storage properties. NiO nanostructures with three distinct morphologies (flower-like, slice-like and particle-like) were fabricated by a sol–gel method. The BET specific surface area of nanoflower, nanoslice, and nanoparticle NiO was 159, 193, and 233 m^2 g^{-1} and the average pore size was 16.7, 6.3, and 8.8 nm, respectively (Fig. 22).[244] With the lowest surface area and largest pore size, the nanoflower NiO nanostructures formed a 3D network, offering the most efficient contact with and transport of the electrolyte. Therefore, this structure granted the best electrochemical properties among three different nanostructures. This study suggests that it is important to facilitate the transport of ions to active materials on the top of large surface area.

3D hierarchical Co_3O_4 twin-spheres with an urchin-like structure were produced by a solvothermal synthesis of cobalt carbonate hydroxide hydrate followed by calcination. The morphology of the precursors evolved from nanorods to sheaf-like bundles, to flower-like structures, to dumbbell-like particles, and eventually to twin-spheres through a three-stage self-assembly of nanorods. Such structure provided larger surface area and better accessibility of electrolytes compared to nanorods and nanodiscs of Co_3O_4. The specific capacitances of the urchin-like structure evaluated from the discharge curves were 781, 754, 700, 670, and 611 F g^{-1} at current densities of 0.5, 1, 2, 4, and 8 A g^{-1}, respectively.[245] Similar urchin-like MnO_2 nanostructures were also produced through a hydrothermal method. It was found that the phase of the products transformed from α-MnO_2 to ε-MnO_2 when Al^{3+} was substituted by Fe^{3+} in the solution. At the same time, the morphology of the product was changed from urchin-like clusters to 3D clew-like structures.[246] The 3D clew-like ε-MnO_2 showed a specific capacitance of 120 F g^{-1} at the scan rate of 5 mV s^{-1}.

Current research in this field focuses on the structural control of the products rather than achieving good electrochemical properties. These nanostructures, although present interesting shapes, have not demonstrated superior performance compared with pseudocapacitive materials deposited on porous carbons and metal foams. In order to advance the application of metal oxide nanostructures in supercapacitors, it is necessary to improve the electrical conductivity, electrolyte accessibility and cycle stability of the materials.

6 Conclusion and outlook

The quest for higher energy and power for supercapacitors to complement or compete with batteries has led to a major effort in developing advanced electrode materials. In this review

article, we overviewed the fabrication and performance of 0–3 dimensional nanostructured electrode materials and discussed the impact of structures on the electrochemical properties. Table 1 exhibits a summary of the properties and characteristics of supercapacitor electrode materials based on various dimensional nanostructures.

For quite some time, 0D materials like activated carbon have been the work horse for developing supercapacitor electrodes. However, the necessity to add an insulating polymer binder to make the actual electrode diminishes its performance. The emergence of perovskites as active materials for solar cell applications has inspired the research of using them for supercapacitor applications. It has been observed that oxygen intercalation in perovskite-type materials can be used to store the charges and has a bright future as the potential material to improve the performance of supercapacitor electrodes. Among other 0D materials, single and multi-shelled hollow structures stand out because of their highly enhanced surface area. 1D nanostructure can also provide efficient transport pathways for both electrons and ions in the supercapacitor electrode. Particularly, binder-free and highly ordered designs can further improve the specific capacitance of the electrodes. Moreover, a rational 1D heterogeneous design helps to achieve enhanced rate capability and cycle stability.

Due to their high surface area, 2D materials offer a unique opportunity to surpass the current limitations of electrode materials. The great advantage of using 2D materials like graphene for supercapacitor application is its high conductivity and large surface area. In order to improve the energy density of pristine graphene-based devices, composites are made with 2D graphenes and conducting polymer or transition metal oxides. This resulted in improved devices with high thermal stability and mechanical strength with minimum restacking of 2D layers. However, stacking of these 2D layers to accomplish a considerable volume poses a major challenge. The availability of a large variety of van der Waals layered materials provides considerable opportunities to develop new 2D materials for future supercapacitor electrodes. Furthermore, MXene, as a new family of 2D materials, shows a great potential for supercapacitor electrode applications.

Building 3D structures with a controlled pore size distribution is very attractive as electrode materials. Utilizing 3D conductive materials as templates and depositing pseudocapacitive materials like conductive polymers and metal oxide on to these 3D structures is a very efficient method to construct high performing supercapacitor electrodes. Composite 3D metal foams are also very promising because of the high electrical conductivity and easy accessibility of electrolyte ions. Assembling prefabricated nanostructures into 3D structures is another very important direction to obtain highly efficient supercapacitor electrodes since nanostructures can be manipulated by controlling synthetic parameters. However, more effort needs to be focused on optimizing the interface between these nanostructures and charge collecting electrodes.

This review is focused on the supercapacitor electrode performance based on the dimensionality of the material used as the electrode. Due to the variability of conditions and parameters used to evaluate the materials, it is not easy to compare the performance of the electrodes with different dimensionality. Nevertheless, we can infer from this review that there are clear advantages and disadvantages for different dimensionalities. For example, it is possible to control the pore size of 0D carbon electrode to less than 10 nm to obtain better electrolyte accessibility than 1D materials, however, the conductivity of 0D materials remains low in the presence of an insulating polymer binder. In the case of 1D materials, it is possible to deposit active materials on a conductive nanowire, but precisely controlling the accessible space between high aspect ratio structures is not a simple task. A feasible future direction is the combination of different dimensionalities to generate a composite which can provide high conductivity, surface area, mechanical and performance stability and capacitance. 2D graphene made into aerogels (3D) with incorporated active nanoparticles like NiO (0D) is an example of such hybrid system. Such composite could also combine the properties of both EDLCs (long cycle life) and pseudocapacitive electrodes (better specific capacitance). Recently, there is a concerted effort to develop 2D materials beyond graphene using van der Waals solids. Many of these solids constitute promising materials for supercapacitor electrodes. It is expected that the combination of these nanomaterials leads to a new generation of supercapacitors electrodes with high energy and power densities in the near future.

Acknowledgements

J.T. acknowledges Florida Space Research Institute and Florida Space Grant Consortium for the financial support.

Notes and references

1 B. E. Conway, *Electrochemical Supercapacitors: Scientific Fundamentals and Technological Applications*, Springer, New York, 1999.
2 P. Simon and Y. Gogotsi, *Nat. Mater.*, 2008, **7**, 845–854.
3 H. Gleiter, *Acta Mater.*, 2000, **48**, 1–29.
4 V. Pokropivny and V. Skorokhod, *Mater. Sci. Eng., C*, 2007, **27**, 990–993.
5 J. N. Tiwari, R. N. Tiwari and K. S. Kim, *Prog. Mater. Sci.*, 2012, **57**, 724–803.
6 L. L. Zhang and X. Zhao, *Chem. Soc. Rev.*, 2009, **38**, 2520–2531.
7 G. Wang, L. Zhang and J. Zhang, *Chem. Soc. Rev.*, 2012, **41**, 797–828.
8 Y. Zhang, H. Feng, X. Wu, L. Wang, A. Zhang, T. Xia, H. Dong, X. Li and L. Zhang, *Int. J. Hydrogen Energy*, 2009, **34**, 4889–4899.
9 W. Wei, X. Cui, W. Chen and D. G. Ivey, *Chem. Soc. Rev.*, 2011, **40**, 1697–1721.
10 M. Zhi, C. Xiang, J. Li, M. Li and N. Wu, *Nanoscale*, 2013, **5**, 72–88.
11 J. Gamby, P. Taberna, P. Simon, J. Fauvarque and M. Chesneau, *J. Power Sources*, 2001, **101**, 109–116.
12 E. Frackowiak, *Phys. Chem. Chem. Phys.*, 2007, **9**, 1774–1785.

13 D.-W. Wang, F. Li, Z.-G. Chen, G. Q. Lu and H.-M. Cheng, *Chem. Mater.*, 2008, **20**, 7195–7200.
14 S. Prabaharan, R. Vimala and Z. Zainal, *J. Power Sources*, 2006, **161**, 730–736.
15 L. Hu, W. Wang, J. Tu, J. Hou, H. Zhu and S. Jiao, *J. Mater. Chem. A*, 2013, **1**, 5136–5141.
16 M. Xue, Z. Xie, L. Zhang, X. Ma, X. Wu, Y. Guo, W. Song, Z. Li and T. Cao, *Nanoscale*, 2011, **3**, 2703–2708.
17 M. P. Yeager, D. Su, N. S. Marinković and X. Teng, *J. Electrochem. Soc.*, 2012, **159**, A1598–A1603.
18 Y.-Z. Zheng, H.-Y. Ding and M.-L. Zhang, *Mater. Res. Bull.*, 2009, **44**, 403–407.
19 Y. Chen, Z. Yu, Y. Chen, L. Luo and X. Wang, *Materials for Renewable Energy & Environment (ICMREE)*, 2011 International Conference on, Shanghai, 2011.
20 X. Du, C. Wang, M. Chen, Y. Jiao and J. Wang, *J. Phys. Chem. C*, 2009, **113**, 2643–2646.
21 C. Liu, F. Li, L. P. Ma and H. M. Cheng, *Adv. Mater.*, 2010, **22**, E28–E62.
22 C. Portet, G. Yushin and Y. Gogotsi, *Carbon*, 2007, **45**, 2511–2518.
23 D. Pech, M. Brunet, H. Durou, P. Huang, V. Mochalin, Y. Gogotsi, P.-L. Taberna and P. Simon, *Nat. Nanotechnol.*, 2010, **5**, 651–654.
24 X. Lang, A. Hirata, T. Fujita and M. Chen, *Nat. Nanotechnol.*, 2011, **6**, 232–236.
25 J. T. Mefford, W. G. Hardin, S. Dai, K. P. Johnston and K. J. Stevenson, *Nat. Mater.*, 2014, **13**, 726–732.
26 X. Lai, J. E. Halpert and D. Wang, *Energy Environ. Sci.*, 2012, **5**, 5604–5618.
27 Z. Zhong, Y.-d. Yin, B. Gates and Y. Xia, *Adv. Mater.*, 2000, **12**, 206–209.
28 B. You, J. Yang, Y. Sun and Q. Su, *Chem. Commun.*, 2011, **47**, 12364–12366.
29 X. Tang, Z.-h. Liu, C. Zhang, Z. Yang and Z. Wang, *J. Power Sources*, 2009, **193**, 939–943.
30 S.-W. Bian, Y.-P. Zhao and C.-Y. Xian, *Mater. Lett.*, 2013, **111**, 75–77.
31 C.-Y. Cao, W. Guo, Z.-M. Cui, W.-G. Song and W. Cai, *J. Mater. Chem.*, 2011, **21**, 3204–3209.
32 W. Yu, X. Jiang, S. Ding and B. Q. Li, *J. Power Sources*, 2014, **256**, 440–448.
33 T. Zhu, Z. Wang, S. Ding, J. S. Chen and X. W. D. Lou, *RSC Adv.*, 2011, **1**, 397–400.
34 Z. Yang, F. Xu, W. Zhang, Z. Mei, B. Pei and X. Zhu, *J. Power Sources*, 2014, **246**, 24–31.
35 Y. Wang, A. Pan, Q. Zhu, Z. Nie, Y. Zhang, Y. Tang, S. Liang and G. Cao, *J. Power Sources*, 2014, **272**, 107–112.
36 X. Lai, J. Li, B. A. Korgel, Z. Dong, Z. Li, F. Su, J. Du and D. Wang, *Angew. Chem., Int. Ed.*, 2011, **50**, 2738–2741.
37 Z. Lei, Z. Chen and X. Zhao, *J. Phys. Chem. C*, 2010, **114**, 19867–19874.
38 Z. Lei, J. Zhang and X. Zhao, *J. Mater. Chem.*, 2012, **22**, 153–160.
39 L. Fan, L. Tang, H. Gong, Z. Yao and R. Guo, *J. Mater. Chem.*, 2012, **22**, 16376–16381.
40 Z.-C. Yang, C.-H. Tang, H. Gong, X. Li and J. Wang, *J. Power Sources*, 2013, **240**, 713–720.
41 Y. Xia, P. Yang, Y. Sun, Y. Wu, B. Mayers, B. Gates, Y. Yin, F. Kim and H. Yan, *Adv. Mater.*, 2003, **15**, 353–389.
42 X. Lu, G. Wang, T. Zhai, M. Yu, J. Gan, Y. Tong and Y. Li, *Nano Lett.*, 2012, **12**, 1690–1696.
43 X. Lu, D. Zheng, T. Zhai, Z. Liu, Y. Huang, S. Xie and Y. Tong, *Energy Environ. Sci.*, 2011, **4**, 2915–2921.
44 X. Lu, G. Wang, T. Zhai, M. Yu, S. Xie, Y. Ling, C. Liang, Y. Tong and Y. Li, *Nano Lett.*, 2012, **12**, 5376–5381.
45 P. Yang, Y. Ding, Z. Lin, Z. Chen, Y. Li, P. Qiang, M. Ebrahimi, W. Mai, C. P. Wong and Z. L. Wang, *Nano Lett.*, 2014, **14**, 731–736.
46 Z. Yu, J. Moore, J. Lorenzo, C. Li and J. Thomas, *ECS Trans.*, 2014, **61**, 31–36.
47 Z. Yu, J. Moore, B. Duong, C. Li and J. Thomas, *ECS Trans.*, 2014, **61**, 49–53.
48 H. Wang, Q. Gao and L. Jiang, *Small*, 2011, **7**, 2454–2459.
49 J. Chen, B. J. Wiley and Y. Xia, *Langmuir*, 2007, **23**, 4120–4129.
50 X. Lu, Y. Zeng, M. Yu, T. Zhai, C. Liang, S. Xie, M. S. Balogun and Y. Tong, *Adv. Mater.*, 2014, **26**, 3148–3155.
51 B. Duong, Z. Yu, P. Gangopadhyay, S. Seraphin, N. Peyghambarian and J. Thomas, *Adv. Mater. Interfaces*, 2014, **1**, 1300014.
52 Z. Yu, B. Duong, D. Abbitt and J. Thomas, *Adv. Mater.*, 2013, **25**, 3302–3306.
53 Z. Yu, C. Li, D. Abbitt and J. Thomas, *J. Mater. Chem. A*, 2014, **2**, 10923–10929.
54 B. Duong, H. Khurshid, P. Gangopadhyay, J. Devkota, K. Stojak, H. Srikanth, L. Tetard, R. A. Norwood, N. Peyghambarian, M. H. Phan and J. Thomas, *Small*, 2014, **10**, 2840–2848.
55 G.-Y. Zhao and H.-L. Li, *Microporous Mesoporous Mater.*, 2008, **110**, 590–594.
56 K. Wang, J. Huang and Z. Wei, *J. Phys. Chem. C*, 2010, **114**, 8062–8067.
57 M. R. Tarasevich and B. N. Efremov, in *Electrodes of Conductive Metallic Oxides Part A*, ed. S. Trasatti, Elsevier, USA, 1982, p. 227.
58 T. Y. Wei, C. H. Chen, H. C. Chien, S. Y. Lu and C. C. Hu, *Adv. Mater.*, 2010, **22**, 347–351.
59 G. Q. Zhang, H. B. Wu, H. E. Hoster, M. B. Chan-Park and X. W. D. Lou, *Energy Environ. Sci.*, 2012, **5**, 9453–9456.
60 H. Xia, J. Feng, H. Wang, M. O. Lai and L. Lu, *J. Power Sources*, 2010, **195**, 4410–4413.
61 C.-C. Hu, K.-H. Chang, M.-C. Lin and Y.-T. Wu, *Nano Lett.*, 2006, **6**, 2690–2695.
62 R. Liu, S. I. Cho and S. B. Lee, *Nanotechnology*, 2008, **19**, 215710.
63 S. Talapatra, S. Kar, S. Pal, R. Vajtai, L. Ci, P. Victor, M. Shaijumon, S. Kaur, O. Nalamasu and P. Ajayan, *Nat. Nanotechnol.*, 2006, **1**, 112–116.
64 D. N. Futaba, K. Hata, T. Yamada, T. Hiraoka, Y. Hayamizu, Y. Kakudate, O. Tanaike, H. Hatori, M. Yumura and S. Iijima, *Nat. Mater.*, 2006, **5**, 987–994.

65 B. Kim, H. Chung and W. Kim, *J. Phys. Chem. C*, 2010, **114**, 15223–15227.
66 C. R. Martin, *Science*, 1994, **266**, 1961–1966.
67 M. P. Zach, K. H. Ng and R. M. Penner, *Science*, 2000, **290**, 2120–2123.
68 E. Menke, M. Thompson, C. Xiang, L. Yang and R. Penner, *Nat. Mater.*, 2006, **5**, 914–919.
69 P.-L. Taberna, S. Mitra, P. Poizot, P. Simon and J.-M. Tarascon, *Nat. Mater.*, 2006, **5**, 567–573.
70 Y. Sun, B. Gates, B. Mayers and Y. Xia, *Nano Lett.*, 2002, **2**, 165–168.
71 Y. Sun, Y. Yin, B. T. Mayers, T. Herricks and Y. Xia, *Chem. Mater.*, 2002, **14**, 4736–4745.
72 S. Vaddiraju, H. Chandrasekaran and M. K. Sunkara, *J. Am. Chem. Soc.*, 2003, **125**, 10792–10793.
73 H. Choi and S.-H. Park, *J. Am. Chem. Soc.*, 2004, **126**, 6248–6249.
74 J. Zhou, N. S. Xu, S. Z. Deng, J. Chen, J. C. She and Z. L. Wang, *Adv. Mater.*, 2003, **15**, 1835–1840.
75 N. Cordente, M. Respaud, F. Senocq, M.-J. Casanove, C. Amiens and B. Chaudret, *Nano Lett.*, 2001, **1**, 565–568.
76 C. Cheng, R. K. Gonela, Q. Gu and D. T. Haynie, *Nano Lett.*, 2005, **5**, 175–178.
77 Y. Lei, B. Daffos, P.-L. Taberna, P. Simon and F. Favier, *Electrochim. Acta*, 2010, **55**, 7454–7459.
78 Z. Su, C. Yang, B. Xie, Z. Lin, Z. Zhang, J. Liu, B. Li, F. Kang and C. Wong, *Energy Environ. Sci.*, 2014, **7**, 2652–2659.
79 J. YoungáKim, *RSC Adv.*, 2012, **2**, 8281–8285.
80 W. Yan, J. Y. Kim, W. Xing, K. C. Donavan, T. Ayvazian and R. M. Penner, *Chem. Mater.*, 2012, **24**, 2382–2390.
81 D. Chao, X. Xia, C. Zhu, J. Wang, J. Liu, J. Lin, Z. Shen and H. J. Fan, *Nanoscale*, 2014, **6**, 5691–5697.
82 Q. Li, Z.-L. Wang, G.-R. Li, R. Guo, L.-X. Ding and Y.-X. Tong, *Nano Lett.*, 2012, **12**, 3803–3807.
83 Z. Yu and J. Thomas, *Adv. Mater.*, 2014, **26**, 4279–4285.
84 L. Bao, J. Zang and X. Li, *Nano Lett.*, 2011, **11**, 1215–1220.
85 P. Yang, X. Xiao, Y. Li, Y. Ding, P. Qiang, X. Tan, W. Mai, Z. Lin, W. Wu, T. Li, H. Jin, P. Liu, J. Zhou, C. P. Wong and Z. L. Wang, *ACS Nano*, 2013, **7**, 2617–2626.
86 X. Sun, Q. Li, Y. Lü and Y. Mao, *Chem. Commun.*, 2013, **49**, 4456–4458.
87 A. Sumboja, X. Wang, J. Yan and P. S. Lee, *Electrochim. Acta*, 2012, **65**, 190–195.
88 G.-R. Li, Z.-L. Wang, F.-L. Zheng, Y.-N. Ou and Y.-X. Tong, *J. Mater. Chem.*, 2011, **21**, 4217–4221.
89 J. Liu, C. Cheng, W. Zhou, H. Li and H. J. Fan, *Chem. Commun.*, 2011, **47**, 3436–3438.
90 J. Yan, E. Khoo, A. Sumboja and P. S. Lee, *ACS Nano*, 2010, **4**, 4247–4255.
91 J. Bae, M. K. Song, Y. J. Park, J. M. Kim, M. Liu and Z. L. Wang, *Angew. Chem., Int. Ed.*, 2011, **50**, 1683–1687.
92 R. K. Sharma, A. Karakoti, S. Seal and L. Zhai, *J. Power Sources*, 2010, **195**, 1256–1262.
93 R. K. Sharma and L. Zhai, *Electrochim. Acta*, 2009, **54**, 7148–7155.
94 Q. Li, J. Liu, J. Zou, A. Chunder, Y. Chen and L. Zhai, *J. Power Sources*, 2011, **196**, 565–572.
95 A. L. M. Reddy, M. M. Shaijumon, S. R. Gowda and P. M. Ajayan, *Nano Lett.*, 2009, **9**, 1002–1006.
96 A. L. M. Reddy, M. M. Shaijumon, S. R. Gowda and P. M. Ajayan, *J. Phys. Chem. C*, 2009, **114**, 658–663.
97 J. Liu, J. Jiang, C. Cheng, H. Li, J. Zhang, H. Gong and H. J. Fan, *Adv. Mater.*, 2011, **23**, 2076–2081.
98 C. Guan, J. Liu, C. Cheng, H. Li, X. Li, W. Zhou, H. Zhang and H. J. Fan, *Energy Environ. Sci.*, 2011, **4**, 4496–4499.
99 X. Xia, J. Tu, Y. Zhang, X. Wang, C. Gu, X.-b. Zhao and H. J. Fan, *ACS Nano*, 2012, **6**, 5531–5538.
100 C. Guan, X. Xia, N. Meng, Z. Zeng, X. Cao, C. Soci, H. Zhang and H. J. Fan, *Energy Environ. Sci.*, 2012, **5**, 9085–9090.
101 X. Xia, D. Chao, Z. Fan, C. Guan, X. Cao, H. Zhang and H. J. Fan, *Nano Lett.*, 2014, **14**, 1651–1658.
102 L. Huang, D. Chen, Y. Ding, S. Feng, Z. L. Wang and M. Liu, *Nano Lett.*, 2013, **13**, 3135–3139.
103 Q. Qu, Y. Zhu, X. Gao and Y. Wu, *Adv. Energy Mater.*, 2012, **2**, 950–955.
104 Q. Li, J. M. Anderson, Y. Chen and L. Zhai, *Electrochim. Acta*, 2012, **59**, 548–557.
105 G. Binotto, D. Larcher, A. Prakash, R. Herrera Urbina, M. Hegde and J.-M. Tarascon, *Chem. Mater.*, 2007, **19**, 3032–3040.
106 G. A. Snook, P. Kao and A. S. Best, *J. Power Sources*, 2011, **196**, 1–12.
107 R. Liu and S. B. Lee, *J. Am. Chem. Soc.*, 2008, **130**, 2942–2943.
108 J. Duay, E. Gillette, R. Liu and S. B. Lee, *Phys. Chem. Chem. Phys.*, 2012, **14**, 3329–3337.
109 X. Xia, D. Chao, X. Qi, Q. Xiong, Y. Zhang, J. Tu, H. Zhang and H. J. Fan, *Nano Lett.*, 2013, **13**, 4562–4568.
110 J.-G. Wang, Y. Yang, Z.-h. Huang and F. Kang, *Electrochim. Acta*, 2014, **130**, 642–649.
111 W. Yao, H. Zhou and Y. Lu, *J. Power Sources*, 2013, **241**, 359–366.
112 L. Mai, F. Dong, X. Xu, Y. Luo, Q. An, Y. Zhao, J. Pan and J. Yang, *Nano Lett.*, 2013, **13**, 740–745.
113 H. Zhang, G. Cao, Z. Wang, Y. Yang, Z. Shi and Z. Gu, *Nano Lett.*, 2008, **8**, 2664–2668.
114 R. Liu, J. Duay and S. B. Lee, *ACS Nano*, 2010, **4**, 4299–4307.
115 R. Mas-Balleste, C. Gomez-Navarro, J. Gomez-Herrero and F. Zamora, *Nanoscale*, 2011, **3**, 20–30.
116 Y. Wang, Z. Shi, Y. Huang, Y. Ma, C. Wang, M. Chen and Y. Chen, *J. Phys. Chem. C*, 2009, **113**, 13103–13107.
117 D. Chen, L. Tang and J. Li, *Chem. Soc. Rev.*, 2010, **39**, 3157–3180.
118 Y. Huang, J. Liang and Y. Chen, *Small*, 2012, **8**, 1805–1834.
119 M. M. Shaijumon, F. S. Ou, L. Ci and P. M. Ajayan, *Chem. Commun.*, 2008, 2373–2375.
120 X. Yang, J. Zhu, L. Qiu and D. Li, *Adv. Mater.*, 2011, **23**, 2833–2838.
121 H. Wang, Y. Liang, T. Mirfakhrai, Z. Chen, H. Casalongue and H. Dai, *Nano Res.*, 2011, **4**, 729–736.
122 K. S. Novoselov, V. I. Falko, L. Colombo, P. R. Gellert, M. G. Schwab and K. Kim, *Nature*, 2012, **490**, 192–200.

123 S. Stankovich, D. A. Dikin, G. H. B. Dommett, K. M. Kohlhaas, E. J. Zimney, E. A. Stach, R. D. Piner, S. T. Nguyen and R. S. Ruoff, *Nature*, 2006, **442**, 282–286.
124 J. Xia, F. Chen, J. Li and N. Tao, *Nat. Nanotechnol.*, 2009, **4**, 505–509.
125 M. D. Stoller, S. Park, Y. Zhu, J. An and R. S. Ruoff, *Nano Lett.*, 2008, **8**, 3498–3502.
126 Q. Qu, S. Yang and X. Feng, *Adv. Mater.*, 2011, **23**, 5574–5580.
127 C. Liu, Z. Yu, D. Neff, A. Zhamu and B. Z. Jang, *Nano Lett.*, 2010, **10**, 4863–4868.
128 J. R. Miller, R. A. Outlaw and B. C. Holloway, *Science*, 2010, **329**, 1637–1639.
129 M. Beidaghi and Y. Gogotsi, *Energy Environ. Sci.*, 2014, **7**, 867–884.
130 J. J. Yoo, K. Balakrishnan, J. Huang, V. Meunier, B. G. Sumpter, A. Srivastava, M. Conway, A. L. Mohana Reddy, J. Yu, R. Vajtai and P. M. Ajayan, *Nano Lett.*, 2011, **11**, 1423–1427.
131 M. Kaempgen, C. K. Chan, J. Ma, Y. Cui and G. Gruner, *Nano Lett.*, 2009, **9**, 1872–1876.
132 Y. Zhu, S. Murali, M. D. Stoller, K. J. Ganesh, W. Cai, P. J. Ferreira, A. Pirkle, R. M. Wallace, K. A. Cychosz, M. Thommes, D. Su, E. A. Stach and R. S. Ruoff, *Science*, 2011, **332**, 1537–1541.
133 A. D. DeYoung, S.-W. Park, N. R. Dhumal, Y. Shim, Y. Jung and H. J. Kim, *J. Phys. Chem. C*, 2014, **118**, 18472–18480.
134 S. Stankovich, D. A. Dikin, R. D. Piner, K. A. Kohlhaas, A. Kleinhammes, Y. Jia, Y. Wu, S. T. Nguyen and R. S. Ruoff, *Carbon*, 2007, **45**, 1558–1565.
135 S. Park, J. An, I. Jung, R. D. Piner, S. J. An, X. Li, A. Velamakanni and R. S. Ruoff, *Nano Lett.*, 2009, **9**, 1593–1597.
136 V. C. Tung, M. J. Allen, Y. Yang and R. B. Kaner, *Nat. Nanotechnol.*, 2009, **4**, 25–29.
137 Y. Zhu, M. D. Stoller, W. Cai, A. Velamakanni, R. D. Piner, D. Chen and R. S. Ruoff, *ACS Nano*, 2010, **4**, 1227–1233.
138 C. Niu, E. K. Sichel, R. Hoch, D. Moy and H. Tennent, *Appl. Phys. Lett.*, 1997, **70**, 1480–1482.
139 C. Du, J. Yeh and N. Pan, *Nanotechnology*, 2005, **16**, 350.
140 H.-J. Shin, K. K. Kim, A. Benayad, S.-M. Yoon, H. K. Park, I.-S. Jung, M. H. Jin, H.-K. Jeong, J. M. Kim, J.-Y. Choi and Y. H. Lee, *Adv. Funct. Mater.*, 2009, **19**, 1987–1992.
141 Y. Si and E. T. Samulski, *Nano Lett.*, 2008, **8**, 1679–1682.
142 W. Lv, D.-M. Tang, Y.-B. He, C.-H. You, Z.-Q. Shi, X.-C. Chen, C.-M. Chen, P.-X. Hou, C. Liu and Q.-H. Yang, *ACS Nano*, 2009, **3**, 3730–3736.
143 A. Burke, *Electrochim. Acta*, 2007, **53**, 1083–1091.
144 W. Gao, N. Singh, L. Song, Z. Liu, A. L. M. Reddy, L. Ci, R. Vajtai, Q. Zhang, B. Wei and P. M. Ajayan, *Nat. Nanotechnol.*, 2011, **6**, 496–500.
145 M. F. El-Kady, V. Strong, S. Dubin and R. B. Kaner, *Science*, 2012, **335**, 1326–1330.
146 Z. Wei, D. Wang, S. Kim, S.-Y. Kim, Y. Hu, M. K. Yakes, A. R. Laracuente, Z. Dai, S. R. Marder, C. Berger, W. P. King, W. A. de Heer, P. E. Sheehan and E. Riedo, *Science*, 2010, **328**, 1373–1376.
147 Y. Zhang, L. Guo, S. Wei, Y. He, H. Xia, Q. Chen, H.-B. Sun and F.-S. Xiao, *Nano Today*, 2010, **5**, 15–20.
148 S. R. C. Vivekchand, C. S. Rout, K. S. Subrahmanyam, A. Govindaraj and C. N. R. Rao, *J. Chem. Sci.*, 2008, **120**, 9–13.
149 C. D. Lokhande, D. P. Dubal and O.-S. Joo, *Curr. Appl. Phys.*, 2011, **11**, 255–270.
150 S. Shi, C. Xu, C. Yang, Y. Chen, J. Liu and F. Kang, *Sci. Rep.*, 2013, **3**, 2598.
151 J. P. Zheng, P. J. Cygan and T. R. Jow, *J. Electrochem. Soc.*, 1995, **142**, 2699–2703.
152 T. P. Gujar, V. R. Shinde, C. D. Lokhande, W.-Y. Kim, K.-D. Jung and O.-S. Joo, *Electrochem. Commun.*, 2007, **9**, 504–510.
153 L. Cao, S. Yang, W. Gao, Z. Liu, Y. Gong, L. Ma, G. Shi, S. Lei, Y. Zhang, S. Zhang, R. Vajtai and P. M. Ajayan, *Small*, 2013, **9**, 2905–2910.
154 B. Lei, G. R. Li and X. P. Gao, *J. Mater. Chem. A*, 2014, **2**, 3919–3925.
155 X. Wang, J. Ding, S. Yao, X. Wu, Q. Feng, Z. Wang and B. Geng, *J. Mater. Chem. A*, 2014, **2**, 15958–15963.
156 J. M. Soon and K. P. Loh, *Electrochem. Solid-State Lett.*, 2007, **10**, A250–A254.
157 K. Krishnamoorthy, G. K. Veerasubramani, S. Radhakrishnan and S. J. Kim, *Mater. Res. Bull.*, 2014, **50**, 499–502.
158 J. Feng, X. Sun, C. Wu, L. Peng, C. Lin, S. Hu, J. Yang and Y. Xie, *J. Am. Chem. Soc.*, 2011, **133**, 17832–17838.
159 M. R. Lukatskaya, O. Mashtalir, C. E. Ren, Y. Dall'Agnese, P. Rozier, P. L. Taberna, M. Naguib, P. Simon, M. W. Barsoum and Y. Gogotsi, *Science*, 2013, **341**, 1502–1505.
160 M. D. Levi, M. R. Lukatskaya, S. Sigalov, M. Beidaghi, N. Shpigel, L. Daikhin, D. Aurbach, M. W. Barsoum and Y. Gogotsi, *Adv. Energy Mater.*, 2014, DOI: 10.1002/aenm.201400815.
161 M. Naguib, M. Kurtoglu, V. Presser, J. Lu, J. Niu, M. Heon, L. Hultman, Y. Gogotsi and M. W. Barsoum, *Adv. Mater.*, 2011, **23**, 4248–4253.
162 M. Naguib, V. N. Mochalin, M. W. Barsoum and Y. Gogotsi, *Adv. Mater.*, 2014, **26**, 992–1005.
163 V. Augustyn, J. Come, M. A. Lowe, J. W. Kim, P.-L. Taberna, S. H. Tolbert, H. D. Abruña, P. Simon and B. Dunn, *Nat. Mater.*, 2013, **12**, 518–522.
164 M. Kurtoglu, M. Naguib, Y. Gogotsi and M. W. Barsoum, *MRS Commun.*, 2012, **2**, 133–137.
165 M. Khazaei, M. Arai, T. Sasaki, C. Y. Chung, N. S. Venkataramanan, M. Estili, Y. Sakka and Y. Kawazoe, *Adv. Funct. Mater.*, 2013, **23**, 2185–2192.
166 Y. Zhang, H. Li, L. Pan, T. Lu and Z. Sun, *J. Electroanal. Chem.*, 2009, **634**, 68–71.
167 S. Yang, G. Cui, S. Pang, Q. Cao, U. Kolb, X. Feng, J. Maier and K. Müllen, *ChemSusChem*, 2010, **3**, 236–239.
168 H. Wang, H. S. Casalongue, Y. Liang and H. Dai, *J. Am. Chem. Soc.*, 2010, **132**, 7472–7477.
169 H. Wang, J. T. Robinson, G. Diankov and H. Dai, *J. Am. Chem. Soc.*, 2010, **132**, 3270–3271.

170 H. Wang, L.-F. Cui, Y. Yang, H. Sanchez Casalongue, J. T. Robinson, Y. Liang, Y. Cui and H. Dai, *J. Am. Chem. Soc.*, 2010, **132**, 13978–13980.
171 Z.-S. Wu, D.-W. Wang, W. Ren, J. Zhao, G. Zhou, F. Li and H.-M. Cheng, *Adv. Funct. Mater.*, 2010, **20**, 3595–3602.
172 H. Xia, Y. S. Meng, G. Yuan, C. Cui and L. Lu, *Electrochem. Solid-State Lett.*, 2012, **15**, A60–A63.
173 T.-S. Hyun, J.-E. Kang, H.-G. Kim, J.-M. Hong and I.-D. Kim, *Electrochem. Solid-State Lett.*, 2009, **12**, A225–A228.
174 J. Zhang, J. Jiang, H. Li and X. S. Zhao, *Energy Environ. Sci.*, 2011, **4**, 4009–4015.
175 Q. Cheng, J. Tang, J. Ma, H. Zhang, N. Shinya and L.-C. Qin, *Carbon*, 2011, **49**, 2917–2925.
176 L. Peng, X. Peng, B. Liu, C. Wu, Y. Xie and G. Yu, *Nano Lett.*, 2013, **13**, 2151–2157.
177 Y. Qian, S. Lu and F. Gao, *J. Mater. Sci.*, 2011, **46**, 3517–3522.
178 Z.-S. Wu, W. Ren, D.-W. Wang, F. Li, B. Liu and H.-M. Cheng, *ACS Nano*, 2010, **4**, 5835–5842.
179 J. Yan, Z. Fan, T. Wei, W. Qian, M. Zhang and F. Wei, *Carbon*, 2010, **48**, 3825–3833.
180 X. Zhao, L. Zhang, S. Murali, M. D. Stoller, Q. Zhang, Y. Zhu and R. S. Ruoff, *ACS Nano*, 2012, **6**, 5404–5412.
181 L. Fenghua, S. Jiangfeng, Y. Huafeng, G. Shiyu, Z. Qixian, H. Dongxue, I. Ari and N. Li, *Nanotechnology*, 2009, **20**, 455602.
182 E. G. da Silveira Firmiano, A. C. Rabelo, C. J. Dalmaschio, A. N. Pinheiro, E. C. Pereira, W. H. Schreiner and E. R. Leite, *Adv. Energy Mater.*, 2014, **4**, 1301380.
183 S. Ratha and C. S. Rout, *ACS Appl. Mater. Interfaces*, 2013, **5**, 11427–11433.
184 S. Li, X. Wang, H. Xing and C. Shen, *J. Micromech. Microeng.*, 2013, **23**, 114013.
185 W. Wang, S. Guo, I. Lee, K. Ahmed, J. Zhong, Z. Favors, F. Zaera, M. Ozkan and C. S. Ozkan, *Sci. Rep.*, 2014, **4**, 4452.
186 Y.-M. Wang, X. Zhang, C.-Y. Guo, Y.-Q. Zhao, C.-L. Xu and H.-L. Li, *J. Mater. Chem. A*, 2013, **1**, 13290–13300.
187 T. Zhai, F. Wang, M. Yu, S. Xie, C. Liang, C. Li, F. Xiao, R. Tang, Q. Wu, X. Lu and Y. Tong, *Nanoscale*, 2013, **5**, 6790–6796.
188 M.-J. Deng, P.-J. Ho, C.-Z. Song, S.-A. Chen, J.-F. Lee, J.-M. Chen and K.-T. Lu, *Energy Environ. Sci.*, 2013, **6**, 2178–2185.
189 X. H. Xia, J. P. Tu, Y. Q. Zhang, Y. J. Mai, X. L. Wang, C. D. Gu and X. B. Zhao, *J. Phys. Chem. C*, 2011, **115**, 22662–22668.
190 C. Zhou, Y. Zhang, Y. Li and J. Liu, *Nano Lett.*, 2013, **13**, 2078–2085.
191 S. Jun, S. H. Joo, R. Ryoo, M. Kruk, M. Jaroniec, Z. Liu, T. Ohsuna and O. Terasaki, *J. Am. Chem. Soc.*, 2000, **122**, 10712–10713.
192 R. Ryoo, S. H. Joo, M. Kruk and M. Jaroniec, *Adv. Mater.*, 2001, **13**, 677–681.
193 H. Hu, Z. Zhao, W. Wan, Y. Gogotsi and J. Qiu, *Adv. Mater.*, 2013, **25**, 2219–2223.
194 W. Xing, S. Z. Qiao, R. G. Ding, F. Li, G. Q. Lu, Z. F. Yan and H. M. Cheng, *Carbon*, 2006, **44**, 216–224.
195 M. Inagaki, H. Konno and O. Tanaike, *J. Power Sources*, 2010, **195**, 7880–7903.
196 D. Zhang, L. Zheng, Y. Ma, L. Lei, Q. Li, Y. Li, H. Luo, H. Feng and Y. Hao, *ACS Appl. Mater. Interfaces*, 2014, **6**, 2657–2665.
197 L. Wang, Y. Zheng, S. Chen, Y. Ye, F. Xu, H. Tan, Z. Li, H. Hou and Y. Song, *Electrochim. Acta*, 2014, **135**, 380–387.
198 H. Jiang, J. Ma and C. Li, *Adv. Mater.*, 2012, **24**, 4197–4202.
199 X. Dong, W. Shen, J. Gu, L. Xiong, Y. Zhu, H. Li and J. Shi, *J. Phys. Chem. B*, 2006, **110**, 6015–6019.
200 Y. Yan, Q. Cheng, G. Wang and C. Li, *J. Power Sources*, 2011, **196**, 7835–7840.
201 Y. G. Wang, H. Q. Li and Y. Y. Xia, *Adv. Mater.*, 2006, **18**, 2619–2623.
202 Y. Yan, Q. Cheng, Z. Zhu, V. Pavlinek, P. Saha and C. Li, *J. Power Sources*, 2013, **240**, 544–550.
203 Z. Lei, X. Sun, H. Wang, Z. Liu and X. S. Zhao, *ACS Appl. Mater. Interfaces*, 2013, **5**, 7501–7508.
204 W.-X. Liu, N. Liu, H.-H. Song and X.-H. Chen, *Carbon*, 2011, **49**, 4610.
205 Y. Yan, Q. Cheng, V. Pavlinek, P. Saha and C. Li, *Electrochim. Acta*, 2012, **71**, 27–32.
206 D. Li, J. Huang and R. B. Kaner, *Acc. Chem. Res.*, 2008, **42**, 135–145.
207 H.-K. Song, Y.-H. Jung, K.-H. Lee and L. H. Dao, *Electrochim. Acta*, 1999, **44**, 3513–3519.
208 G.-J. Lee and S.-I. Pyun, *Langmuir*, 2006, **22**, 10659–10665.
209 H. Yamada, H. Nakamura, F. Nakahara, I. Moriguchi and T. Kudo, *J. Phys. Chem. C*, 2006, **111**, 227–233.
210 A. J. Amali, J.-K. Sun and Q. Xu, *Chem. Commun.*, 2014, **50**, 1519–1522.
211 S. Kubo, R. J. White, K. Tauer and M.-M. Titirici, *Chem. Mater.*, 2013, **25**, 4781–4790.
212 Q. Long, W. Chen, H. Xu, X. Xiong, Y. Jiang, F. Zou, X. Hu, Y. Xin, Z. Zhang and Y. Huang, *Energy Environ. Sci.*, 2013, **6**, 2497–2504.
213 M. Oschatz, L. Borchardt, K. Pinkert, S. Thieme, M. R. Lohe, C. Hoffmann, M. Benusch, F. M. Wisser, C. Ziegler, L. Giebeler, M. H. Ruemmeli, J. Eckert, A. Eychmueller and S. Kaskel, *Adv. Energy Mater.*, 2014, **4**, 1300645.
214 Q. Zhao, X. Wang, C. Wu, J. Liu, H. Wang, J. Gao, Y. Zhang and H. Shu, *J. Power Sources*, 2014, **254**, 10–17.
215 D.-W. Wang, F. Li, M. Liu, G. Q. Lu and H.-M. Cheng, *Angew. Chem., Int. Ed.*, 2008, **47**, 373–376.
216 S. Dutta, A. Bhaumik and K. C. W. Wu, *Energy Environ. Sci.*, 2014, **7**, 3574–3592.
217 B. Xu, S. Hou, G. Cao, M. Chu and Y. Yang, *RSC Adv.*, 2013, **3**, 17500–17506.
218 R. Liu, J. Duay and S. B. Lee, *Chem. Commun.*, 2011, **47**, 1384–1404.
219 D. Lan, Y. Chen, P. Chen, X. Chen, X. Wu, X. Pu, Y. Zeng and Z. Zhu, *ACS Appl. Mater. Interfaces*, 2014, **6**, 11839–11845.
220 C. Yuan, J. Li, L. Hou, J. Lin, X. Zhang and S. Xiong, *J. Mater. Chem. A*, 2013, **1**, 11145–11151.
221 J. Luo, H. D. Jang, T. Sun, L. Xiao, Z. He, A. P. Katsoulidis, M. G. Kanatzidis, J. M. Gibson and J. Huang, *ACS Nano*, 2011, **5**, 8943–8949.

222 J. Luo, H. D. Jang and J. Huang, *ACS Nano*, 2013, **7**, 1464–1471.
223 Y. Xu, Z. Lin, X. Zhong, X. Huang, N. O. Weiss, Y. Huang and X. Duan, *Nat. Commun.*, 2014, **5**, 4554.
224 Y. Zhu, S. Murali, W. Cai, X. Li, J. W. Suk, J. R. Potts and R. S. Ruoff, *Adv. Mater.*, 2010, **22**, 3906–3924.
225 Z. Yu, M. McInnis, J. Calderon, S. Seal, L. Zhai and J. Thomas, *Nano Energy*, DOI: 10.1016/j.nanoen.2014.11.030.
226 Z.-S. Wu, A. Winter, L. Chen, Y. Sun, A. Turchanin, X. Feng and K. Muellen, *Adv. Mater.*, 2012, **24**, 5130–5135.
227 B. G. Choi, M. H. Yang, W. H. Hong, J. W. Choi and Y. S. Huh, *ACS Nano*, 2012, **6**, 4020–4028.
228 X. Ma, J. Liu, C. Liang, X. Gong and R. Che, *J. Mater. Chem. A*, 2014, **2**, 12692–12696.
229 X. Jiang, X. Yang, Y. Zhu, J. Shen, K. Fan and C. Li, *J. Power Sources*, 2013, **237**, 178–186.
230 X. Zhu, P. Zhang, S. Xu, X. Yan and Q. Xue, *ACS Appl. Mater. Interfaces*, 2014, **6**, 11665–11674.
231 S. Wu, W. Chen and L. Yan, *J. Mater. Chem. A*, 2014, **2**, 2765–2772.
232 J. T. Zhang, S. Liu, G. L. Pan, G. R. Li and X. P. Gao, *J. Mater. Chem. A*, 2014, **2**, 1524–1529.
233 Q. Wu, Y. Xu, Z. Yao, A. Liu and G. Shi, *ACS Nano*, 2010, **4**, 1963–1970.
234 J. Xu, K. Wang, S.-Z. Zu, B.-H. Han and Z. Wei, *ACS Nano*, 2010, **4**, 5019–5026.
235 X. Yu, B. Lu and Z. Xu, *Adv. Mater.*, 2014, **26**, 1044–1051.
236 F. Zhang, D. Zhu, X. a. Chen, X. Xu, Z. Yang, C. Zou, K. Yang and S. Huang, *Phys. Chem. Chem. Phys.*, 2014, **16**, 4186–4192.
237 X. Xie, C. Zhang, M.-B. Wu, Y. Tao, W. Lv and Q.-H. Yang, *Chem. Commun.*, 2013, **49**, 11092–11094.
238 L. Zhang, F. Zhang, X. Yang, G. Long, Y. Wu, T. Zhang, K. Leng, Y. Huang, Y. Ma, A. Yu and Y. Chen, *Sci. Rep.*, 2013, **3**, 1408.
239 Y. Shao, H. Wang, Q. Zhang and Y. Li, *J. Mater. Chem. C*, 2013, **1**, 1245–1251.
240 G. K. Dimitrakakis, E. Tylianakis and G. E. Froudakis, *Nano Lett.*, 2008, **8**, 3166–3170.
241 F. Du, D. Yu, L. Dai, S. Ganguli, V. Varshney and A. K. Roy, *Chem. Mater.*, 2011, **23**, 4810–4816.
242 Z.-Y. Yang, Y.-F. Zhao, Q.-Q. Xiao, Y.-X. Zhang, L. Jing, Y.-M. Yan and K.-N. Sun, *ACS Appl. Mater. Interfaces*, 2014, **6**, 8497–8504.
243 Q. Li, J. M. Anderson, Y. Chen and L. Zhai, *Electrochim. Acta*, 2012, **59**, 548–557.
244 S.-I. Kim, J.-S. Lee, H.-J. Ahn, H.-K. Song and J.-H. Jang, *ACS Appl. Mater. Interfaces*, 2013, **5**, 1596–1603.
245 Y. Xiao, S. Liu, F. Li, A. Zhang, J. Zhao, S. Fang and D. Jia, *Adv. Funct. Mater.*, 2012, **22**, 4052–4059.
246 P. Yu, X. Zhang, D. Wang, L. Wang and Y. Ma, *Cryst. Growth Des.*, 2009, **9**, 528–533.